A newcomer's guide to ultrashort pulse shaping and characterization

PhD TUTORIAL

A newcomer's guide to ultrashort pulse shaping and characterization

Antoine Monmayrant[1,2]**, Sébastien Weber**[3] **and Béatrice Chatel**[3]

[1] CNRS-LAAS, 7 avenue du colonel Roche, F-31077 Toulouse, France
[2] Université de Toulouse, UPS, INSA, INP, ISAE ; LAAS, F-31077 Toulouse, France
[3] CNRS-Université de Toulouse; UPS, Laboratoire Collisions, Agrégats Réactivité, IRSAMC, F-31062 Toulouse, France.

E-mail: beatrice.chatel@irsamc.ups-tlse.fr

Abstract

This tutorial gives an overview of the most widespread techniques of both ultrashort pulse shaping and pulse characterization.

(Some figures in this article are in colour only in the electronic version)

1. Introduction

In 1966, a few years after the first laser came to light, short picosecond pulses became available [1]. Their generation and characterization were already active fields of research. Forty-four years later, few-cycle femtosecond pulses and complex shaped pulses can be synthesized in various spectral regions. These arbitrarily shaped optical waveforms are of great interest in a number of fields including coherent control [2–4], multidimensional spectroscopy [5], biological imaging [6], compression of optical pulses [7], factorization of numbers [8, 9] and optical communications [10]. Most of these works were spurred by technological breakthroughs in the field of arbitrary pulse shaping [11]. This spectacular progress has been obtained in parallel with the development of new tools for a complete characterization of ultrashort pulses [12, 13]. We propose to describe for newcomers to the field the basics of arbitrary pulse shaping and pulse characterization. The tone of this tutorial is to be as didactic as possible and is intentionally not a complete review. To help beginners, several tables and numerical applications enlighten the text. The authors strongly recommend that interested readers should read more extensive articles such as Weiner's review [11] of pulse shaping or the recent review on characterization by Walmsley and Dorrer [13]. Finally, the present work is complemented by a range of interesting books [14–16].

This tutorial is organized as follows: section 2 gives some mathematical background for the description and representation of ultrashort pulses, section 3 is devoted to arbitrary pulse shaping, section 4 presents some of the most widespread methods for ultrashort pulse characterization and section 5 gives an overview of shaping-assisted characterization.

2. Definition of the electric field and its representation

2.1. Definition of the electric field

A laser pulse is entirely defined by its electric field $\mathcal{E}(t)$. For ultrashort pulses however, $\mathcal{E}(t)$ is not easily accessed and the spectral domain is often more practical. As $\mathcal{E}(t)$ is a real function, its Fourier transform reads $\tilde{\mathcal{E}}(\omega) = 1/2(\tilde{E}(\omega) + \tilde{E}^*(-\omega))$ where $\tilde{E}(\omega)$ is the complex electric field taking non-zero values only for positive values of the frequency ω.

$\tilde{E}(\omega)$ is a complex function containing all the information concerning the pulse and from which $\mathcal{E}(t)$ can be retrieved. From the inverse Fourier transform of $\tilde{E}(\omega)$ one gets a complex field in the temporal domain $E(t)$, whose real part is $\text{Re}[E(t)] = \mathcal{E}(t)$:

$$\mathcal{E}(t) = \int_{-\infty}^{+\infty} \tilde{\mathcal{E}}(\omega) \exp(-\mathrm{i}\omega t) \frac{\mathrm{d}\omega}{2\pi}. \qquad (1)$$

The shape of an ultrashort pulse can thus be defined equivalently by its electric field $\mathcal{E}(t)$, or by its complex electric
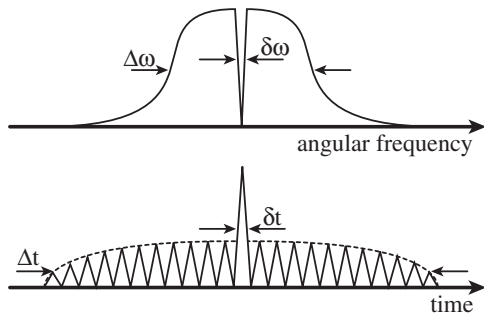
Figure 1. The complexity can be seen as the ratio between the largest and smallest features in either time or spectral domains. Δt and δt (resp. $\Delta \omega$ and $\delta \omega$) are the largest and smallest features in the time (resp. in spectral) domain.

field in the time domain $E(t)$ or in the spectral domain $\tilde{E}(\omega)$. $\tilde{E}(\omega) = A(\omega)e^{i\varphi(\omega)}$ is usually the most practical definition and both its spectral amplitude $A(\omega)$ and its spectral phase $\varphi(\omega)$ contribute to the pulse shape. As an example, for a given spectral amplitude, the spectral phase alone completely determines the pulse duration and shape. The shortest duration is achieved for a flat phase and the pulse is said to be *Fourier limited*. When a pulse is Fourier limited, its duration is inversely proportional to its spectral width. When it is no longer Fourier limited, its duration increases. The time–bandwidth product (TBP) provides a way to estimate how far a pulse is from the Fourier limit. The TBP is the product of time duration and spectral width of a given pulse:

$$\text{TBP} = \Delta t \cdot \Delta \omega \qquad (2)$$

where Δt and $\Delta \omega$ are the full width at half maximum (FWHM) in intensity of the pulse temporal and spectral profiles[4]. Another way to estimate the distance from Fourier limited is the complexity [11]. It can be interpreted as the ratio between the largest and the smallest features in either the time or spectral domains:

$$\eta = \Delta t / \delta t = \Delta \omega / \delta \omega \qquad (3)$$

as sketched in figure 1. The TBP and complexity are proportional and for a Gaussian spectrum one obtains

$$\eta \simeq \text{TBP} / 4 \ln 2. \qquad (4)$$

The spectral phase plays a central role in determining the complexity, and more generally the shape, of a short pulse. There are several quantities related to the spectral phase that are often used to describe the evolution of a shaped pulse. The group delay is defined as $T_g(\omega) = \partial \varphi / \partial \omega$ and it describes the arrival time of each spectral component of the pulse. The instantaneous frequency, defined as $\omega(t) = \partial \varphi_t / \partial t$ (where φ_t is the temporal phase), gives the opposite point of view as it describes the temporal evolution of the frequency of the short pulse. Both can be extremely useful to grasp the main characteristics of a given shaped pulse.

Expanding the spectral phase as a Taylor series is another useful tool to analyse the effect of each term of the series:

----

[4] We arbitrarily choose to work with the FWHM.

$$\varphi(\omega) = \varphi_0^{(0)} + \varphi_0^{(1)}(\omega - \omega_0) + \frac{1}{2}\varphi_0^{(2)}(\omega - \omega_0)^2$$
$$+ \frac{1}{6}\varphi_0^{(3)}(\omega - \omega_0)^3 + \frac{1}{24}\varphi_0^{(4)}(\omega - \omega_0)^4$$
$$+ \cdots + \frac{1}{n!}\varphi_0^{(n)}(\omega - \omega_0)^n \qquad (5)$$

with $\varphi_0^{(0)} = \varphi(\omega_0)$ and $\varphi_0^{(n)} = (d^n \varphi / d\omega^n)_{\omega_0}$.

- $\varphi_0^{(0)}$ is known as the absolute phase, or the carrier envelope phase (CEP), which corresponds to the phase between the envelope of the electric field and the carrier. This phase plays a key role in nonlinear interactions such as high harmonic generation when pulses are short enough that only a few cycles lie within the envelope (cf figure 2). However, in this tutorial, we consider many-cycle pulses and we do not focus on the CEP. Interested readers can refer to [17] for CEP measurement and control.
- $\varphi_0^{(1)}$ simply corresponds to a delay between the pulse and an arbitrary origin of time. This leads to a constant group delay.
- $\varphi_0^{(2)}$ is the most famous term, well known as *chirp*. It induces an increase of the pulse duration. Around any given frequency under the pulse spectrum, the quadratic phase can be approximated by its tangent, whose slope is simply the group delay which evolves linearly with the frequency. In other words, each frequency experiences a delay that linearly increases as we scan through the spectrum, as shown in figure 3(b). For a strong chirp ($\varphi_0^{(2)} \gg \Delta t_{TF}^2$, where Δt_{TF} is the Fourier-limited pulse duration), the instantaneous frequency is given by $\omega(t) = \omega_0 + t / \varphi_0^{(2)}$. Many experiments have been performed to study the interaction of atoms or molecules with a chirped pulse leading to fascinating results [18–21].
- $\varphi_0^{(3)}$ corresponds to the cubic phase. It leads in the temporal domain to many pre- or post-pulses (figure 3(c)) and can be exploited in coherent control schemes [22]. When aiming for really short pulses, cubic phase as well as higher orders has to be properly compensated.

It is worth noting that some phases cannot be expanded as a Taylor series, such as sinusoidal phases or phase jumps that are routinely used in coherent control schemes.

2.2. How to represent a short pulse?

The most common way to represent a short pulse is to plot both its spectral amplitude $A(\omega)$ and its spectral phase $\varphi(\omega)$ as shown in the first column of figure 3 for a flat phase, a $\varphi_0^{(2)}$, a $\varphi_0^{(3)}$, a π-jump and a two-pulse sequence. Another possibility is to plot the temporal intensity[5] $|E(t)|^2$, as shown in the second column of figure 3.

However, in some cases, time-domain or frequency-domain representations are not enough, especially when both time and frequency properties are strongly coupled. Time–frequency distributions such as the Wigner function have

----

[5] This time representation does not carry all the information on the pulse as the oscillations under the envelope are not shown.
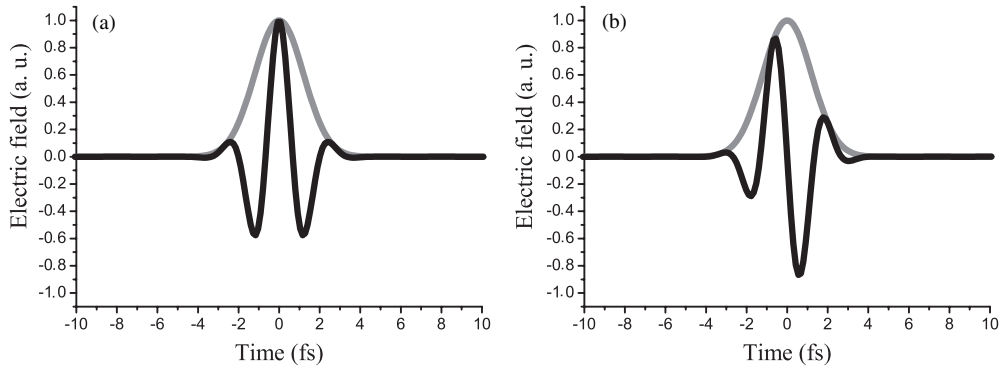
Figure 2. $\mathcal{E}(t)$ (in black) and envelope (in grey) of the electric field of a short laser pulse in two cases of carrier envelope phase. The pulse has a central wavelength of 800 nm and a FWHM of 2 fs. In (a) a 0 rad CEP shows a cosine pulse and in (b) a $\pi/2$ rad CEP shows a sine pulse.
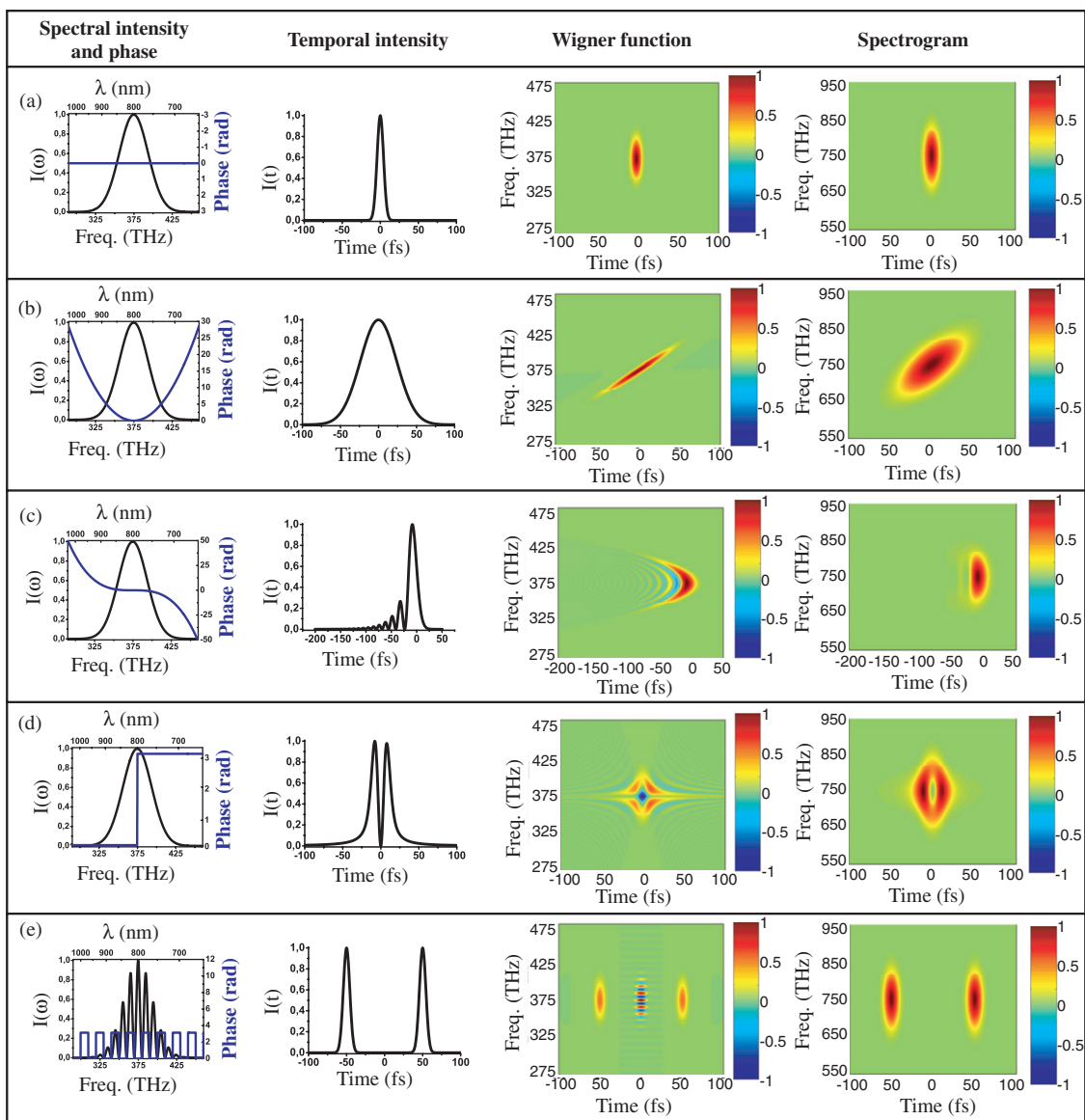

Figure 3. Pulse shaping gallery: (a) Fourier transform pulse, (b) chirped pulse, (c) cubic phase, (d) spectral π-jump, (e) two-pulse sequence. The first column presents the spectral intensity and phase, the second one, the temporal intensity, the third one the Wigner function and the last one the spectrogram. The gate chosen for it is a Fourier-limited 10 fs pulse at 800 nm.

3

been proposed to provide an intuitive mapping of these time–frequency couplings [23, 24]. The Wigner function of an electric field $E(t)$ can be written as [24]

$$W(t, \omega) = \int E\left(t + \frac{t'}{2}\right) E^*\left(t - \frac{t'}{2}\right) e^{i\omega t'} dt' \qquad (6)$$

or alternatively using its spectral electric field $\tilde{E}(\omega)$:

$$W(t, \omega) = \frac{1}{2\pi} \int \tilde{E}\left(\omega + \frac{\omega'}{2}\right) \tilde{E}^*\left(\omega - \frac{\omega'}{2}\right) e^{-i\omega' t} d\omega'. \quad (7)$$

The equivalence of these two definitions can be shown using Fourier transform properties. The third column of figure 3 shows the Wigner functions for different pulse shapes. As an example, for $\varphi_0^{(2)}$ (case (b)), one can clearly see the linear sweep in time of the instantaneous frequency. Although it contains all the information on the pulse and usually provides an intuitive representation for complex pulse, the Wigner function can sometimes be difficult to interpret. As an example, for a two-pulse sequence (case (e)), there are fringes and a maximum around $t = 0$ although there is no energy at that time in the two-pulse sequence. For the case of two pulses or cubic phase, the Wigner function can be negative. The marginals, however, which represent the temporal and spectral intensity of the pulse, are always positive [13]. A more intuitive alternative to the Wigner function is the spectrogram that can be written as

$$S(t, \omega) = \left| \int E(t') g(t' - t) e^{i\omega t'} dt' \right|^2 \qquad (8)$$

The spectrogram is the time convolution of the electric field with a gate $g(t)$ that can be the pulse itself. In the last column of figure 3, the spectrogram of each case is plotted: the gate chosen is a Fourier-limited pulse at 800 nm with a FWHM duration of 10 fs. Some well-known complete characterization techniques retrieve the spectrogram [25].

3. Arbitrary pulse shaping of ultrashort pulses

3.1. Generalities

The use of optimally shaped pulses to guide and control the temporal evolution of a system has been an active field of research for the last 20 years. Two main approaches have been developed.

In the absence of predesigned control mechanisms a closed loop scheme [26–34] may be employed to find efficient pulse shapes: the outcomes of many different shapes are fed back into an algorithm that iteratively optimizes the excitation shape without insight into the physical mechanism that is triggered by a particular shape.

In contrast, the effect of shapes on model systems can be systematically studied within an open-loop scheme [35–40]. This open-loop approach is well adapted to small systems for which theoretical predictions are reliable. It consists of reaching a specific goal (manipulation of the temporal response of a system excited by a light pulse) without any experimental feedback. Physical analysis of the process allows predetermination of the theoretical pulse shape that leads to
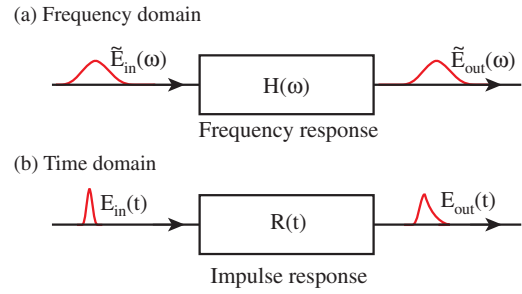

Figure 4. Pulse shaping by linear filtering: (a) frequency domain and (b) time domain.

the desired result. It is then implemented experimentally. Some results by 'test-error' have also been obtained in complex systems following this open-loop approach [41].

Recently researchers have tried to combine both approaches to retrieve information from the complex pulses designed by the closed-loop approach [42, 43]. In particular, interesting results have been obtained in the strong field domain [44–47].

This field has pushed new developments, in particular to extend the pulse shaper's capabilities

- in terms of the refresh rate, which is crucial in the closed-loop approach,
- in terms of the time shaping window to extend the size of the phase space,
- in terms of the spectral bandwidth to be able to control a great variety of systems, and so on.

In this section we will present the basics and some key results. We will insist on the most fundamental principles, limitations and experimental advice to allow newcomers in the field to develop and correctly use their own device.

Pulse shaping techniques presented here are based on the linear, time-invariant filter. They can be described either in the time domain or in the frequency domain.

In the time domain, the output of a linear filter (cf figure 4) is simply given by the following convolution product:

$$E_{out}(t) = R(t) \otimes E_{in}(t) \qquad (9)$$

where $R(t)$ is the impulse response of the pulse shaper. However, for femtosecond pulses, direct shaping in time is quite a hard task and most of the devices operate in the spectral domain and the output pulse can be written as
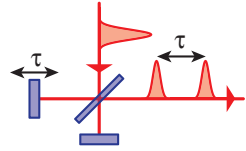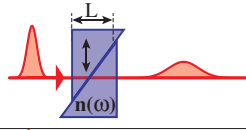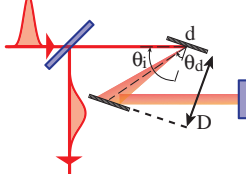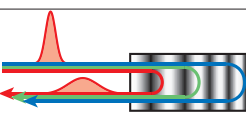
$$\tilde{E}_{out}(\omega) = H(\omega) \tilde{E}_{in}(\omega) \qquad (10)$$

where the transfer function $H(\omega)$ completely describes the pulse shaper.

In the past decade, a lot of effort was put into developing versatile pulse shapers based on programmable masks. Many programmable pulse shapers are now available but none is universal: they are all complex systems with extremely diverse ranges of usage. All currently available programmable pulse shapers address the pulse spectral components by spatially separating them. Thus, they necessarily introduce a spatio-temporal coupling (see section 3.2.3).

In order to buy or develop the right pulse shaper for a given experiment, we recommend listing its requirements in terms of

Table 1. Simple shaping set-ups. (a) Michelson interferometer producing two delayed pulses, (b) propagation through a dispersive bulk medium (length L, index n), (c) grating compressor (θ_i incident angle, θ_d diffraction angle, D distance between the two gratings and d the interline spacing) and (d) chirped mirror (in a chirped mirror, the penetration depth depends on the wavelength which introduces chirp on a Fourier-limited pulse). The first column gives a schematic of the set-up, the second column its transfer function and the last column gives a few references.

(a)	$H(\omega) = \frac{1}{2}\left(1 + e^{i\omega\tau}\right)$	for example [48]
(b)	$H(\omega) = e^{i\phi(\omega)}$ $\phi(\omega) = n(\omega)L\omega/c$	[49]
(c)	$H(\omega) = e^{i\phi(\omega)}$ $\phi(\omega) = 2\frac{\omega}{c}D\frac{\cos(\theta_i+\theta_d)}{\cos\theta_i}$	[50, 51, 49]
(d)	$H(\omega) = \lvert H(\omega)\rvert e^{i\phi(\omega)}$ $\lvert H(\omega)\rvert$ is the reflectivity $\phi(\omega)$ designed until the fourth order	[52, 53]

central frequency, tunability, spectral bandwidth, complexity and maximum duration of the shaped pulse, power density, repetition rate, etc. From this list one can sort the available solutions according to their suitability to the experiment requirements. This may reveal that a programmable pulse shaper is not necessary and that the required waveforms may easily be produced using usual optics. In particular if the complexity η (see section 2.1) of the desired shape is above a few hundred, it exceeds the possibilities of current pulse shapers, as we will see below. As an example, two pulses of 20 fs separated by 60 ps leads to a complexity of 3000! Fortunately, this is easily achievable using a Michelson interferometer. Table 1 summarizes the main devices which may be more appropriate, for some specific shapes, even if they are less versatile than a programmable pulse shaper.

3.2. A spatial mask in the Fourier plane of a zero dispersion line

3.2.1. Introduction. In 1983, Froehly and co-workers [54] proposed a new design of versatile pulse shaper, the so-called *zero dispersion line* or *4f-line*.

A $4f$-line is a particular spectrometer composed of two diffraction gratings and two lenses arranged in a $4f$ set-up, where the CCD camera is replaced by a mask (cf figure 5). Each spectral component is angularly dispersed by the first grating, then is focused to small diffraction spots in the Fourier plane by the first lens (or mirror). Thus, in this plane, all the spectral components are spatially separated and focused. Then a second combination of lens (or curved mirror) and grating allows the recombination of all the frequencies into a single collimated beam. If nothing is placed in the Fourier plane then the device is dispersion free (zero dispersion
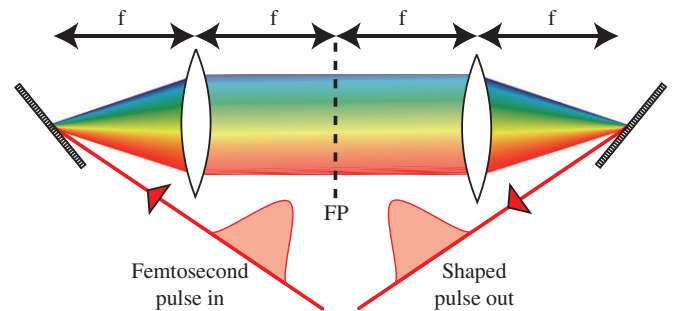
Figure 5. A zero dispersion line composed of two gratings and two lenses of focal length f, arranged in a $4f$ set-up. The output pulse is identical to the input pulse. In the Fourier plane FP, all the spectral components are spatially separated and focused.

line) and the output pulse shape is identical to the input one. By putting a specific mask in the Fourier plane, one can modify the optical path and/or optical density for each spectral component and thus shape the output pulse. For ultrashort pulses (broad spectral bandwidth), the lenses are often replaced by cylindrical or spherical mirrors to avoid unwanted dispersion and chromatic aberrations. Depending on the mask, a $4f$ pulse shaper controls the phase [11], both phase and amplitude [55], the polarization [56] and also the transverse spatial profile [57].

3.2.2. 4f-line theory in a few equations. We present here the basic equations that govern $4f$-line abilities for shaping [58]. We consider the input pulse to be Gaussian in both time and space, with a central frequency ω_0 (corresponding to a central wavelength λ_0), and with the following FWHM in intensity:
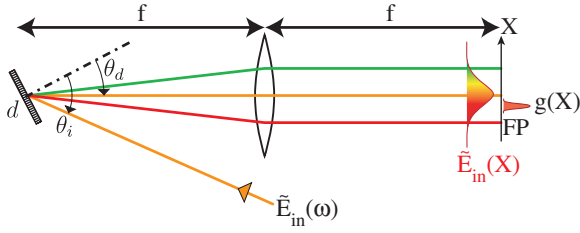
Figure 6. Half a $4f$-line : the Fourier plane is situated in the back focal plane of the lens. f is the focal length. X is the spatial coordinate in this plane. $g(X)$ is the spatial extension of a given frequency component. θ_i is the incident angle on the grating. d is the grating period. θ_d is the diffraction angle.

- $\Delta\omega_L$ in the spectral domain,
- Δt in the temporal domain[6],
- Δx_{in} in the spatial domain[7].

As shown in figure 6, the input pulse is diffracted by the first grating with an angle θ_d at λ_0 (θ_i being the input angle), d is the grating period and f the focal length. In the Fourier plane, each spectral component has a finite size Δx_0 due to diffraction. It is easily derived from Gaussian beam propagation:

$$\Delta x_0 = 2\ln(2)\frac{\cos\theta_i}{\cos\theta_d}\frac{f\lambda_0}{\pi\Delta x_{\text{in}}}. \tag{11}$$

Let us now consider the spatial coordinate X in the Fourier plane. Assuming linear dispersion, a frequency ω_k is located in the Fourier plane at X_k given by

$$X_k = \alpha\omega_k \tag{12}$$

where α is set by the $4f$-line geometry:

$$\alpha = \frac{\lambda_0^2 f}{2\pi cd\cos\theta_d}. \tag{13}$$

The frequency resolution is easily obtained from equations (12) and (13):

$$\delta\omega = \Delta x_0/\alpha. \tag{14}$$

Through the Fourier transform, this corresponds to a window T in the time domain

$$T = 4\ln(2)/\delta\omega = \Delta x_{\text{in}}/|v| \tag{15}$$

where $|v|$ has the dimension of velocity:

$$v = cd\cos\theta_i/\lambda_0. \tag{16}$$

T is the time window available for shaping and equation (15) clearly states that it is proportional to the input waist. This unexpected property of the $4f$-line is a manifestation of spatio-temporal coupling (see section 3.2.3 for more details) and v is usually called the spatio-temporal coupling velocity. T defines a temporal upper bound for shaping achievable with such a $4f$-line: the duration or the time delay of the shaped pulse should stay below T; otherwise strong distortions will occur. The temporal lower bound is given by the inverse of the

spectral bandwidth of the input pulse, which means that the shaper's shortest feature is governed by the available optical bandwidth[8].

Numerical applications

- In the IR [60], gratings: $1/d = 2000\,\text{gr mm}^{-1}$; $f = 600\,\text{mm}$; beam diameter $\Delta x = 2\,\text{mm}$, incident angle $\theta_i = 64°$, $\lambda_0 = 800\,\text{nm}$, $\Delta\lambda_L = 10\,\text{nm}$. This leads to a temporal window $T \simeq 24\,\text{ps}$ and a complexity $\eta \simeq 255$.
- In the mid-IR [61], $1/d = 300\,\text{gr mm}^{-1}$; $f = 125\,\text{mm}$; incident angle (Littrow configuration) $\theta_i = 47°$, $\Delta x_0 = 250\,\mu\text{m}$, $\lambda_0 = 4900\,\text{nm}$, $\Delta t = 140\,\text{fs}$. This leads to a temporal window $T \simeq 78\,\text{ps}$ and a complexity $\eta \simeq 557$.

To turn a $4f$-line into a pulse shaper, we put a mask in its Fourier plane. It has a number of control parameters which can be pixels or not. Then to maximize pulse shaping capability, one should fulfil the following constraint:

$$\text{control parameter number} \geqslant \eta \tag{17}$$

This mask will act both as a spatial mask M_X and a spectral mask M_ω. Immediately after the mask, the pulse can be written as

$$\tilde{E}_{\text{after}}(\omega, X) = \tilde{E}_{\text{in}}(\omega)\cdot g(X - \alpha\omega)M_X(X) \tag{18}$$

where

$$g(X) = \exp[-2\ln(2)(X/\Delta x_0)^2] \tag{19}$$

is the spatial extension of a given frequency component. As the position and frequency are coupled in the Fourier plane, both the spectral and spatial components of the pulse are affected by the mask. As a result, propagating the pulse through the second half of the pulse shaper requires special care and goes beyond simple Gaussian propagation. Setting this aside using Gaussian propagation gives a linear expression for the output pulse $\tilde{E}_{\text{out}}(\omega)$:

$$\tilde{E}_{\text{out}}(\omega) = H(\omega)\tilde{E}_{\text{in}}(\omega) \tag{20}$$

where

$$H(\omega) = \int M_{\omega'}g(\omega' - \omega)\text{d}\omega' = M_\omega \otimes g(\omega) \tag{21}$$

and $M_\omega(\omega) = M_X(\alpha\omega)$. To obtain this expression, we have implicitly assumed that the spatial profile is unaffected by the mask, which is a strong simplification. As a consequence, this expression is only valid for sufficiently smooth and simple shapes and for the on-axis part of the pulse (that remains after a subsequent spatial filtering).

An illustration of the effect of the time window T is given in figure 7(c) that shows the intensity trace of a pulse delayed using a $4f$ pulse shaper. As the programmed delay moves away from 0, the pulse peak intensity decreases and follows a Gaussian envelope of FWHM in intensity of around 24 ps, which corresponds to the temporal window T [60].

---

[6] Time and frequency FWHM in intensity verify the following inequality: $\Delta t\Delta\omega_L \geqslant 4ln(2)$.

[7] It is related to the waist w_{in} of the beam at the input of the $4f$-line, by $\Delta x_{\text{in}} = w_{\text{in}}\sqrt{2\ln(2)}$

[8] It is possible to obtain a shorter pulse than the Fourier-limited one by shaping the spectral amplitude. The cost is the appearance of a pedestal in the time domain as well as a decrease of energy [59].
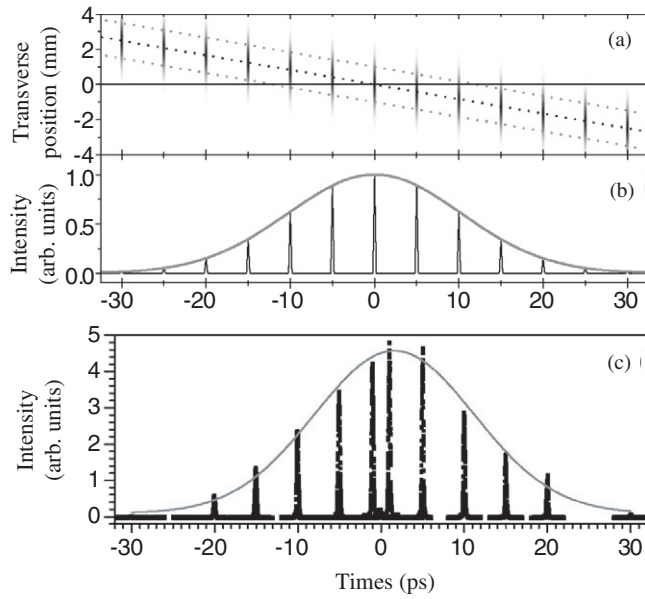
Figure 7. Space-time coupling in the case of a delay: (a) theoretical plot versus time and transverse position of a shaped pulse for various programmed delays. (b) Cross-section of the plot (a) along the axis of propagation (transverse position = 0). (c) Experimental cross-correlations of shaped pulses for various delays.

3.2.3. Spatio-temporal coupling. Let us describe more precisely the way the 4*f*-line acts on the beam. The first grating couples each frequency ω into a given direction k_ω and the first lens (or mirror) maps k_ω to a given position X_ω in the Fourier plane. As a result, the position X_ω in the Fourier plane corresponds both to a certain spectral component and to a certain direction (i.e. a certain spatial frequency). The part of the mask lying at X_ω thus acts simultaneously on both ω and k_ω and this is the origin of the spatio-temporal coupling. After going through the second half of the 4*f*-line, all the components are recombined. At the output of the pulse shaper, the net result of spatio-temporal coupling is that the transverse profile of the beam is modulated according to the temporal shape of the pulse.

For example in the case of a delay, the mask is a linear spectral phase applied to both frequencies and spatial frequencies. The shaped pulse is thus shifted in time, but also shifted along the transverse coordinate. This is illustrated in figure 7(a) where we have plotted the pulse profile versus time (horizontal axis) and space (vertical axis) for various programmed delays: as the delay is changed, the pulse appears to move along a slanted line (black dash) whose slope is precisely the spatio-temporal coupling speed v. Several articles [62–64], including recent ones [65, 66] have covered spatio-temporal coupling in detail.

Spatio-temporal coupling is inherent to all programmable pulse shapers and in particular 4*f*-line pulse shapers and cannot be avoided, in particular when asking for complex waveforms or when pushing a 4*f* pulse shaper to its limits. One simple test to determine if spatio-temporal coupling is negligible is if one is able to shape the phase without affecting the amplitude of the pulse (a π-step spectral phase could be

a good test as demonstrated in [64]). However, its effect can be reduced by designing a 4*f*-line with a spatio-temporal coupling speed v as small as possible. Impressive results have been obtained in an open-loop coherent control approach which clearly demonstrate that this effect is not detrimental for these experiments [36, 38].

3.3. Most common masks

Nowadays different kinds of masks can be placed in the Fourier plane of a 4*f*-line to form a pulse shaper. We propose to describe in more detail the liquid crystal and the acousto-optic modulator masks, which are the most commonly used in the field. Some others are also available and will be briefly mentioned afterwards. For all these masks, one important parameter is the total refresh time which is the time required to obtain a given programmable waveform. This time includes the loading time depending on the data transfer mode (USB, GPIB, etc) and the physical refreshing time depending on the mask itself (for example, orientation of the liquid crystal, travelling time of the acoustic wave, movements of the actuators, etc).

3.3.1. Liquid crystal masks. Each pixel of a liquid crystal spatial light modulator (LC-SLM) is a programmable waveplate controlled by voltage. An LC-SLM consists of a thin layer of nematic liquid crystal placed between two glass substrates. One substrate is covered with transparent ITO (indium tin oxide) electrodes which allow the application of independent voltages to each pixel. The nematic liquid crystals are small rods which are oriented parallel to the substrate when no voltage is applied. Their anchorage direction is fixed by brushing of the electrodes. When a voltage is applied, the nematic molecules tend to align along the field. This modifies the birefringence of the medium, leading to a modification of the optical path for light polarized along the anchorage direction. For a frequency ω, the pixel acts as a waveplate whose phase ϕ is given by

$$\phi(\omega, U) = \frac{\omega \Delta n(\omega, U) e_{CL}}{c} \tag{22}$$

where $\Delta n(\omega, U)$ is the index difference between the slow and fast axes, U is the applied voltage and e_{CL} is the liquid crystal thickness. The pixels have a typical width of $97\,\mu$m with a gap of $3\,\mu$m (cf figure 8(a)). This gap is not really controlled and will lead to undesirable effects (see below).

To achieve amplitude and phase shaping, two spatial light modulators are needed with the anchorage direction at $+45°$ and $-45°$ with respect to the horizontal axis. By placing horizontal polarizers at both the input and output of the 4*f*-line, the complex transfer function of one particular pixel k can be written as

$$H_k = \exp\left(i\frac{\phi_1(\omega_k) + \phi_2(\omega_k)}{2}\right) \cos\left(\frac{\phi_1(\omega_k) - \phi_2(\omega_k)}{2}\right) \tag{23}$$

where ω_k is the frequency impinging on pixel k. ϕ_1 and ϕ_2 correspond respectively to the phase introduced by the first and second LC-SLM. With the same set-up, it is also possible to shape phase and polarization, by removing all the polarizers [56]. In that case, however, one should keep in mind that most
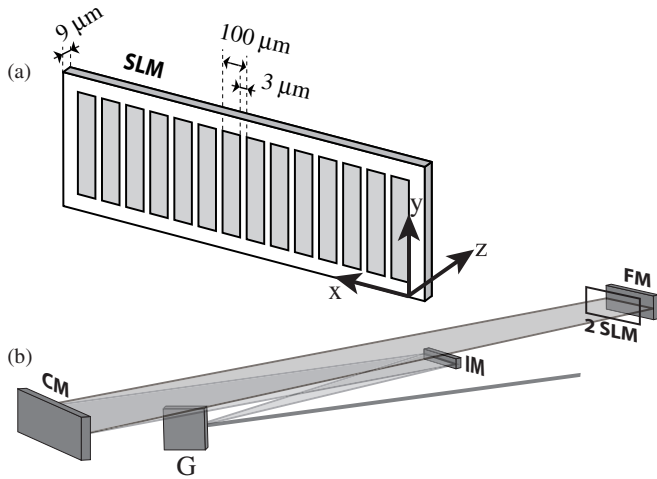
Figure 8. (a) 640 pixel liquid crystal spatial light modulator. (b) A folded zero dispersion line geometry with almost no optical aberration. G: grating; IM: intermediate mirror; CM: cylindrical mirror; FM: folding mirror; SLM: liquid crystal mask.

of the usual optics (mirrors, beamsplitter, gratings, etc) are polarizing elements that can alter the waveform.

Alignment and calibration. The performance and accuracy of the pulse shaper are strongly correlated to the quality of the alignment and the calibration. At least three steps are necessary to obtain a reliable pulse shaper that can be used in an open-loop experiment. We will describe these steps for a $4f$-line fitted with two LC-SLMs (to shape both phase and amplitude).

- The first step consists of a careful alignment of the $4f$-line. This step depends on the chosen geometry and optical components. Several geometries with varying degrees of compacity and optical aberrations [60, 67–70] have been used. We will focus on the folded geometry [60] as depicted in figure 8(b) as it is easy to align and almost aberration-free. In this line, distances are such that the grating is in the front focal plane of the cylindrical mirror and the folding mirror in its back focal plane. The input beam is first diffracted by the grating G, and then sent to the cylindrical mirror CM via an intermediate flat mirror IM. The cylindrical mirror focuses each spectral component to a given transverse position in the Fourier plane. A folding mirror FM is placed in this plane and sends everything back with a small vertical tilt. The mask is situated as close as possible to the Fourier plane [63] (it should stay within the Rayleigh range). The final step for the alignment is to check that the device is really a zero dispersion line by measuring both input and output pulse durations (either autocorrelation or a self-referenced technique can be used as mentioned in section 4 on characterization techniques).
- The second step is to calibrate the introduced phase $\phi(\omega, U)$ as a function of both voltage and frequency, for each LC-SLM. In principle, each pixel should be calibrated independently and at the specific frequency that impinges on it. In practice however, the process is
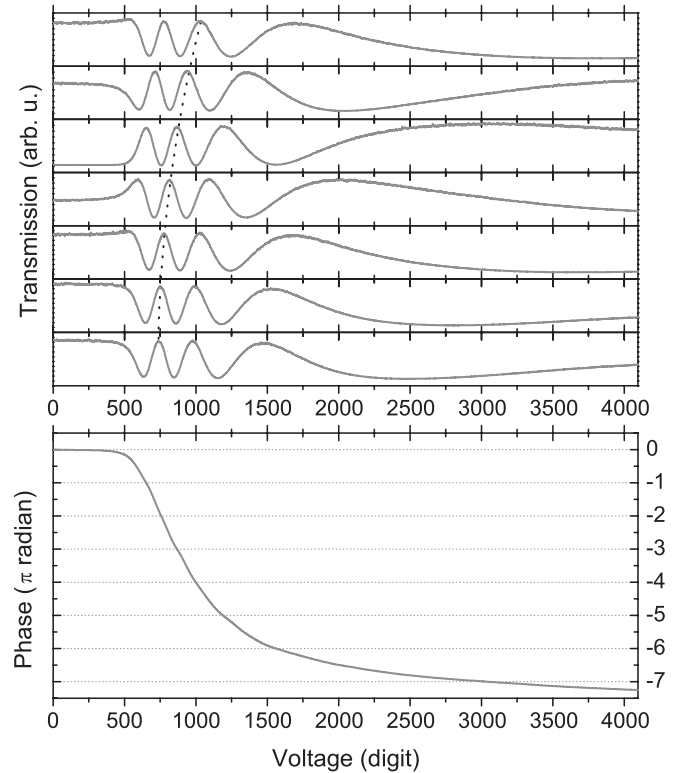

Figure 9. Phase-voltage calibration at 795 nm of a CRI-128 LC-SLM. Top curves: transmitted intensity as a function of the applied voltage, for several orientation of the waveplate; the position of the extrema depends on the extra phase added by the waveplate (dashed line is a guide to the eye). Bottom curve: reconstructed phase as a function of the voltage.

much simpler. First, the LC-SLM is usually homogeneous enough to use a unique voltage calibration for all the pixels. Second, from the voltage calibration at one specific frequency ω_{cal}, we can derive the voltage calibration for any frequency:

$$\phi(\omega, U) = \phi(\omega_{\mathrm{cal}}, U) \cdot \frac{\omega}{\omega_{\mathrm{cal}}} \cdot \frac{\Delta n(\omega, 0)}{\Delta n(\omega_{\mathrm{cal}}, 0)}. \qquad (24)$$

A simple way to calibrate the phase is to place the LC-SLM between two horizontal polarizers, illuminate with a monochromatic laser at ω_{cal} and measure the transmitted intensity I_{cal} as a function of the voltage U applied to all the pixels of the mask[9]. From equation (23), we get that $I_{\mathrm{cal}}(U) \propto [\cos(\phi(\omega_{\mathrm{cal}}, U)/2)]^2$. In theory, it is easy to invert this relation and retrieve $\phi(\omega_{\mathrm{cal}}, U)$. In practice however, problems arise at each extremum of $I_{\mathrm{cal}}(U)$ where the retrieved phase gets noisy and highly distorted. To overcome this difficulty, a waveplate is added next to the LC-SLM to introduce a variable phase ϕ_{wp} so that the transmitted intensity now reads:

$$I_{\mathrm{cal}}(U, \phi_{wp}) \propto [\cos(\phi(\omega_{\mathrm{cal}}, U)/2 + \phi_{wp}/2)]^2 \qquad (25)$$

By repeating the voltage calibration for various ϕ_{wp}, we get a set of transmission curves with shifted extrema as shown in figure 9, top curves. By combining the

---

[9] In the case of a dual LC-SLM, each LC-SLM is calibrated independently, while the second one is switched off.

retrieved phase from each curve we obtain a phase–voltage calibration that is distortion-free across the whole voltage range as shown on the bottom curve of figure 9.

- The last step is to calibrate the dispersion of the pulse shaper, i.e. the mapping (X_k, ω_k). The nonlinear dispersion law is known and can be written as

$$X(\omega_k) - X_0 = f \cdot \tan\left[\arcsin\left(\frac{2\pi c}{\omega_k d} - \sin(\theta_i) \right) \right.$$
$$\left. - \arcsin\left(\frac{2\pi c}{\omega_0 d} - \sin(\theta_i) \right) \right] \qquad (26)$$

where X_k is the position of the kth pixel, ω_k is the frequency on the pixel k, X_0 is the position of the central frequency, ω_0 is the central frequency, f is the focal length, d is the grating period and θ_i is the incident angle. The adjusted parameters in the experiment are X_0 and θ_i. Practically, we measure the spectrum of the output beam using a well-calibrated spectrometer with at least the same spectral resolution as the $4f$-line. To pair the frequency ω_k with the pixel k, we program a zero transmission at the pixel k or a π-jump between the pixels k and $k + 1$. This leads to a hole in the spectrum that is easy to spot. Knowing the dispersion law (equation (26)), ten points across the spectrum are sufficient to precisely calibrate the spatial dispersion in the Fourier plane. This calibration is required each time the alignment of the $4f$-line is modified.

Results. The LC-SLMs have been among the first arbitrary masks used in a $4f$-line. They have been widely and successfully used in a broad range of application as pulse compression [71], coherent control with high/low repetition rate lasers [3, 33–38], biological imaging [6], in quantum optics [40] and recently to cool molecules [72] but also to control ablation processes [73].

Thanks to their wide transparency windows, they can be used on a broad spectral range from the IR to the UV (cf table 2). They have been carefully studied by several groups and used to do spectral phase shaping, as well as phase and amplitude [11] or polarization shaping [56]. They are commercially available and sold by several companies leading to a variety in terms of geometrical aperture, number of pixels, refresh rate, anti-reflection coatings. Table 2 outlines some of the available devices, given some technical characteristics as the number of pixels, the type of control, the damage threshold, etc.

To illustrate the abilities of the LC-SLM $4f$-line, experimental data obtained with our high-resolution pulse shaper [60] are shown in figure 10. It is composed of one pair each of reflective gratings (with 2000 gr mm^{-1}) and cylindrical mirrors ($f = 600$ mm). Its active elements—two 640 pixel LC-SLMs from Jenoptik—are installed in the Fourier plane. This provides a high resolution of 0.06 nm/pixel [60], with a typical 24 ps time window. The shortest temporal feature obtained in this experiment is 94 fs. In figure 10, three examples are presented: (a) three equal amplitude pulse pairs with relative intensity 1/2:1:1/3, (b) a square pulse of 700 fs and (c) three pulses with cubic, flat and quadratic phase. In
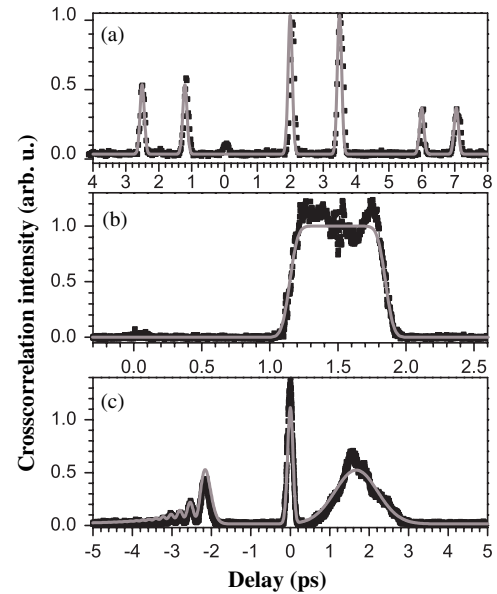

Figure 10. Three experimental waveforms (black dots) are presented: (a) three equal amplitude pulses pairs with relative intensity 1/2:1:1/3, (b) a square pulse of 700 fs, and (c) three pulses with cubic, flat and quadratic phase. The solid grey line is the analytical desired waveform intensity.

each example, black dots correspond to the experimental result whereas the solid grey line is the target analytical waveform. The effects of gaps and the spatial profile (Gaussian temporal envelope) are almost compensated for in the applied mask.

Limitations. As mentioned above, inside the gaps of a pixelated LC-SLM, the phase is not controlled. In a first approximation the LCs behave as if there were no applied voltage. All the gaps thus have the same transmission and a small fraction of the whole spectrum is transmitted through the gaps, leading in the time domain to a small replica of the input beam at $t = 0$, clearly visible in figure 11(a), where a chirped pulse has been programmed. It is possible to compensate for this gap replica by programming a replica of similar intensity but in opposite phase: they will cancel each other by destructive interference. As the behaviour in the gaps is not controlled, an iterative procedure is often needed [63] to find the right compensation replica.

The second main limitation is the pixellization. Pixels are regular discrete elements. Their width in the spectral domain is denoted $\delta\omega$. The mask thus induces a discretized transfer function in the frequency domain. By Fourier transform, the impulse response is a periodic function [74] with a period $T_{\text{rep}} = 2\pi/\delta\omega$. Figure 11(b) presents two examples of delayed pulses which have been programmed at $\simeq 15$ ps and $\simeq 20$ ps using our high-resolution pulse shaper [60]. For each one a chirped replica appears respectively at $\simeq -20$ ps and $\simeq -15$ ps, which correspond to the period $T_{\text{rep}} \approx 35$ ps. This value is in agreement with the pixel size in the spectral domain $\delta\lambda = 0.06$ nm (i.e. $\delta\omega \approx 0.177$ rad ps^{-1}). The replica is chirped due to the nonlinear dispersion in the Fourier plane. However, the Gaussian temporal window (due to the spatial profile in the Fourier plane) will attenuate the replicas situated close to the edge of the window.

Table 2. Summary of available spatial light modulators for $4f$-line based pulse shapers and few characteristics used in experiments of cited references. LC: liquid crystal, AOM: acousto-optic modulator, MEMM: micro-electro mechanical mirrors, MMDM: micro-machined deformable mirror and 2D LC: a 2D liquid crystal device. λ_0 is the laser source wavelength used in the references, the *control type* shows for which shaping SLM can be used, *parameter number* is the independent points of control of the mask. The *efficiency* is the transmission (LC), diffraction (AOM) or reflection coefficient. The *refreshing rate* gives the refreshing pattern frequency of the mask and finally the *damage threshold* is indicated with the source used for its evaluation. NA: characteristic not available.

| Mask	Ref	λ_0 (nm)	Control type	Param. number	Efficiency	Refresh. rate (Hz)	Damage threshold (GW cm^{-2})
LC (pixelated)	[97]	400	Amplitude	2*648	85%	~10	>1.3 (395 nm, 30 fs)
	[69]	Vis	Phase	2*128	85%		4 (890 nm, 50 fs)
	[60]	800	Polarization	2*640	95%		300 (800 nm, 45 fs)
AOM	[89]	260		170	78%	~10^5	Fused silica: NA
	[78]	400		200	NA		
	[98]	Vis	Amplitude	900	NA		TeO$_2$: 0.1
	[76]	800	Phase	900	30–90%		
	[61]	4900		500	80%		Germanium: NA
MEMM (pixelated)	[93]	266	Phase	240*200	NA	~10^2	Aluminium coating
	[92]	400		240*200	85%		
MMDM	[90]	800	Phase	3*13	97%	~10^3	Gold coating
2D LC (pixelated)	[95]	805	Amplitude	480*480	~50%	NA	NA
	[96]	800	Phase	1920*1080	~55%	60	NA
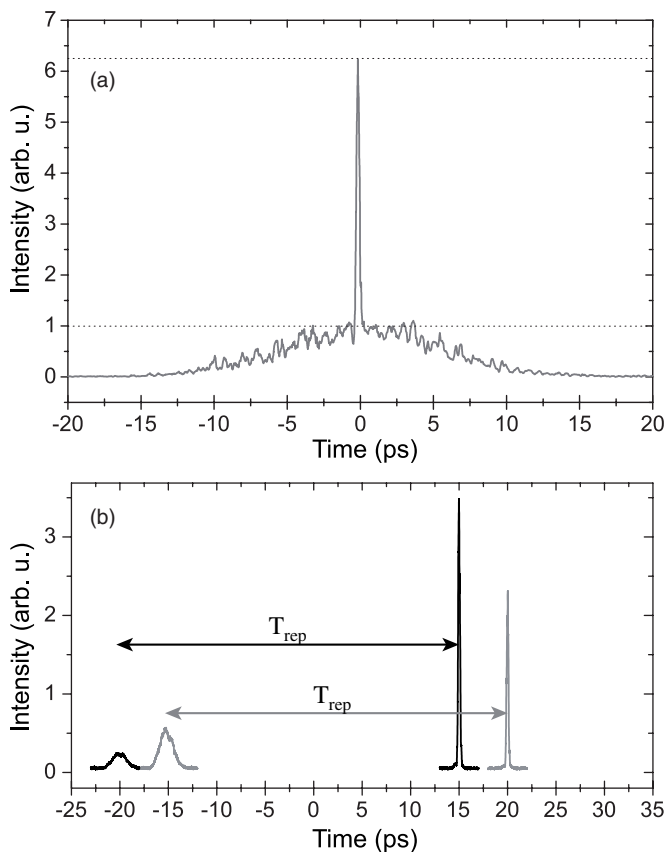
Figure 11. (a) Cross-correlation of a chirped pulse with a reference ultrashort pulse. The gap-replica is clearly visible. (b) Cross-correlation of two delayed pulses: +15 ps (black solid line) and +20 ps (grey solid line); replicas due to the pixellization of the mask are clearly seen respectively around −20 ps and −15 ps. Their temporal broadening is due to the nonlinear dispersion in the Fourier plane. $T_{\rm rep}$ is the period of the replicas, given by the spectral pixel size.

To exploit the spatial resolution of the mask, the incident frequency components should be focused to a spot size comparable with or less than the pixel width. If the spot size is too small, replica waveforms that arise from discrete Fourier sampling will not be attenuated. If the spot size is too big, the blurring of the mask will give rise to substantial diffraction effects [63].

Finally, as mentioned above, the physical refreshing time is defined as the time required by the liquid crystal to be oriented (hundreds of μs). Contrary to acousto-optic devices that rely on a travelling wave (see the next section), once oriented, the LCs stay still and the waveform is stationary. This means that the physical refreshing time does not limit the repetition rate of the laser. LCs are often used with oscillator sources, although may not be operated on a shot-to-shot basis.

3.3.2. Acousto-optic modulator masks. An acousto-optic modulator (AOM) to be used as a SLM has been developed by Warren and co-workers [75, 76] in 1994. The spatial mask pattern is driven by a temporal radiofrequency voltage signal, and converted into a travelling acoustic wave by a piezoelectric transducer [77]. Scaled into space by the acoustic velocity ($v_{\rm ac}$) in the AOM crystal, it acts as a refractive index grating. The grating period is given by the local wavelength of the acoustic waveform ($\Lambda = v_{\rm ac}/\nu$) where ν is the RF drive frequency. This waveform can be simultaneously phase-, amplitude- and frequency-modulated through appropriate RF synthesis. Each spatially dispersed frequency component is then diffracted (see figure 12) with the appropriate phase and amplitude which leads to the desired Fourier transform pulse shaping.

The acousto-optic effect is based on a parametric interaction [77]. As in the parametric effect case, a phase matching condition has to be fulfilled. The efficiency of diffraction in different orders is given by the phase mismatch
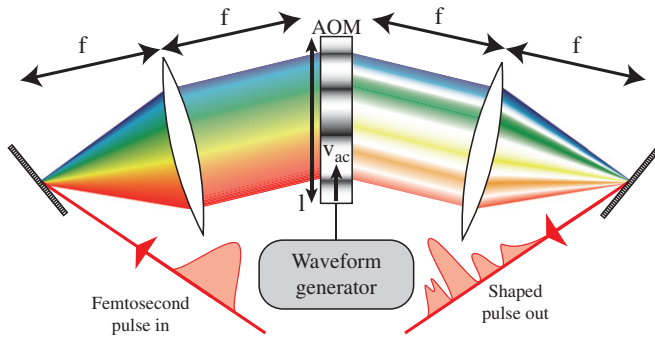
Figure 12. Programmable pulse shaper based on the use of a $4f$-line and an acousto-optic modulator. A radiofrequency wave is generated and converted to an acoustic wave by a piezoelectric modulator. This travelling wave acts as a diffractive grating mask. v_{ac} is the acoustic wave velocity; l is the aperture of the AOM.

δ_m between the diffracted wave in the mth order and the free acoustic and optical waves:

$$\delta_m \propto \Delta k_m L \propto Q \left(m - \frac{\sin \theta_0}{\sin \theta_B} \right) \tag{27}$$

with the Bragg angle given by

$$\sin \theta_B = \frac{\lambda_0}{2n\Lambda}. \tag{28}$$

This angle maximized the first-order diffraction. n is the refractive index and L is the thickness of the crystal, λ_0 is the optical wavelength, Λ is the acoustic wavelength and θ_0 is the incident angle of the optical wave on the acousto-optical modulator. Q is a dimensionless parameter, usually used to classify AOM regimes. It is defined by

$$Q = 2\pi \frac{L}{L_{eff}} = \frac{2\pi \lambda_0 L}{n \Lambda^2} \tag{29}$$

where L_{eff} is an effective length.

- In the Raman–Nath regime, the AOM is described as a thin grating $L \ll L_{eff}$ which corresponds to $Q \leqslant 1$. This leads to a good phase matching for the different orders as can be seen on equation (27). Moreover, it has been shown that the efficiency scales quadratically with acoustic amplitude [76]. This regime allows the best spatial resolution but a limited efficiency of around 30%.
- For $Q \geqslant 4\pi$, which means $L \gg L_{eff}$, the AOM works in the Bragg regime. Once again, regarding equation (27), the mismatch will increases dramatically with the order of diffraction. Phase matching for the first order is obtained at the Bragg angle. In this regime, the efficiency could in principle reach 90%.

A good compromise between efficiency and resolution for pulse shaping application appears for $Q \simeq 4\pi$ [76].

Alignment and calibration. The first step to use the shaper consists of a careful alignment of the $4f$-line as for LC-SLM. Then the AOM is placed in the Fourier plane and tilted until it reaches the Bragg incidence angle. For TeO$_2$ ($\lambda_0 = 780$ nm, $n = 2.26$, $v_{ac} = 4.2 \times 10^3$ m s^{-1} and $\nu = 200$ MHz), this gives $\theta_B = 0.47°$ inside the crystal corresponding to 1.1° in air [76].
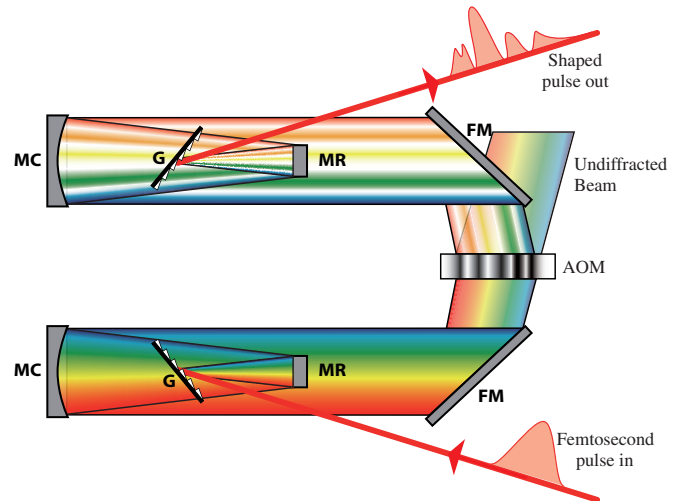

Figure 13. Experimental set-up of a $4f$-line with an AOM spatial mask. A first alignment of the line is done without the AOM. In a second step, the folded mirrors (FM) are used to compensate for the AOM deflection. The first one is used to enter the AOM at the Bragg angle whereas the second is used to compensate for the diffraction angle.
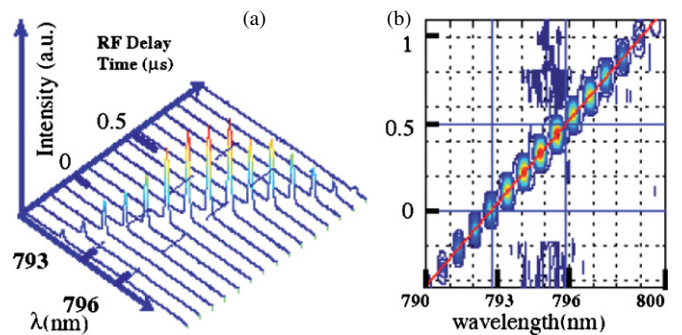

Figure 14. Taken from [79]. Calibration curves for AOM pulse shaper. (A) Each line represents a shaped spectrum created with a short RF pulse delayed in time in the AOM. Each delay corresponds to a different spatial position on the AOM leading to a different spectral position. This figure is used to calibrate the pulse shaper response function with respect to amplitude and time. (B) Data from A viewed as a contour plot. The solid red line fits the data; the coordinates are then used to calibrate the RF time with respect to the optical wavelength.

The second grating should be moved to compensate for the diffraction. The set-up, shown in figure 13, is particularly well suited for AOM masks [61, 78]. Its advantage is the presence of two folding mirrors at each side of the AOM, which allows an easy compensation of the tilt induced by the AOM.

The next step is to calibrate the RF time versus the optical frequency and leads to a mask function $M(\omega) = f(t_{RF} = \alpha\omega)$. The procedure of this experimental calibration is detailed in [79]. An experimental trace is shown in figure 14.

Results. First let us briefly describe the main operating characteristics of an AOM (a complete overview can be found in [76]).
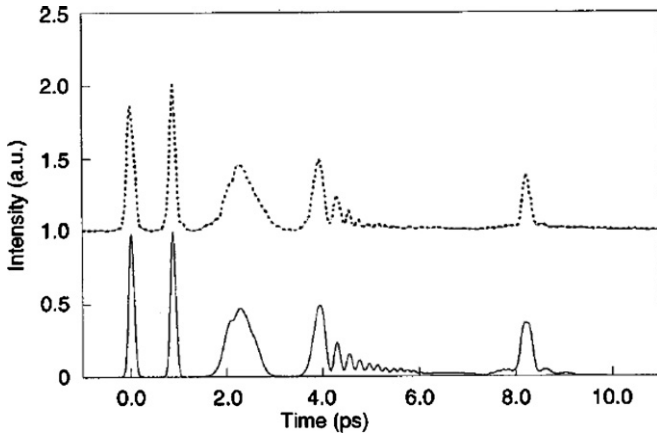
Figure 15. Taken from [76]. Dashed line: intensity cross-correlation trace of a shaped femtosecond pulse using AOM-SLM. The waveform used consists of an initial Fourier-limited pulse followed in time by pulses shaped with linear, quadratic, cubic and quartic spectral phase. Solid line: theoretical trace.

- The refreshing rate is limited by the travelling time of the acoustic wave across the modulator aperture l (figure 12). For TeO_2 (typical AOM crystal used in the visible and the NIR), the acoustic velocity is $v_{ac} = 4.2 \, \text{mm} \, \mu s^{-1}$. In [76], the modulator has a 4.3 cm aperture, which leads to a corresponding time aperture[10] $\Delta\tau = l/v_{ac} = 10 \, \mu s$. With such parameters, the diffraction pattern can then be updated on the microsecond time scale.
- The shortest resolution available is now given by the shortest acoustic feature size δx, which can be compared to a pixel in LC-SLM. The number of control parameters is given by an effective number of pixels:

$$N_{pix}^{eff} = \frac{l}{\delta x} = \Delta\tau \, \Delta f \qquad (30)$$

where Δf is the modulation bandwidth of the AOM, and l is the AOM aperture. It leads to approximately 900 effective pixels in [76]. The real resolution of the shaper is given by the combination of N_{pix}^{eff} and $4f$-line properties described above. The typical complexity already obtained experimentally is in the order of few hundreds (around 200 for [78] and 500 for [61]).

Several groups [80–84] have performed optimal control with this mask whose refresh rate can be as high as 100 kHz for a typical AOM shaper. It has also been used for pulse compression [78, 80, 85] as well as coherent control [86, 87] and for multidimensionnal spectroscopy [5, 85, 88]. Several materials with acousto-optic properties are commercially available which allows the exploration of a very broad spectral range from the UV using fused silica [78, 89] to the mid-IR using germanium [61]. In this spectral range, it is probably the best technique for pulse shaping.

Figure 15 [76] shows an example of complex phase and amplitude shaping. The source is a femtosecond oscillator with an 82 MHz repetition rate; a pulse picker reduces it to 20 kHz (the acoustic refresh rate is in the order of

---

[10] This time is, for the acoustic device, the physical refreshing time defined above.

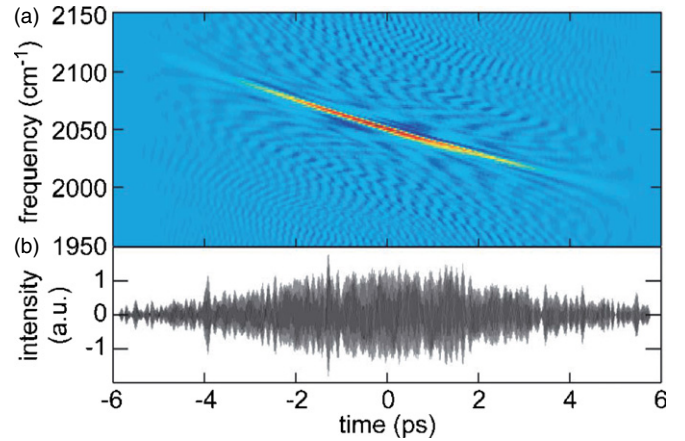**Figure 16.** Taken from [61]. (a) Wigner diagram obtained from (b). (b) Cross-correlation of a linearly chirped shaped pulse at 4.87 μm or 2050 cm^{-1} in the mid IR.
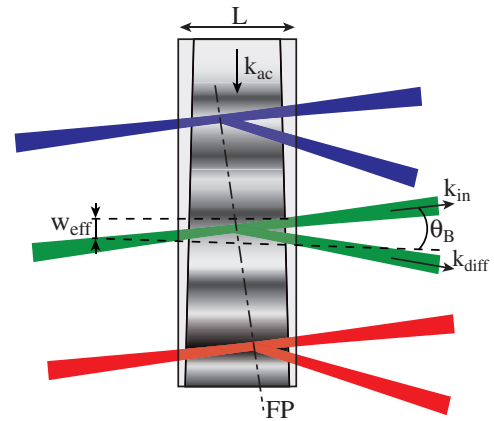
Figure 17. Illustration of the limitations due to the geometry and the thickness of the interaction. The spectrum is dispersed along the vertical direction and three monochromatic frequency components are plotted. To keep the same spatial resolution across the thickness L of the AOM, the average diameter of the beam w_{eff} must be less than the minimum acoustic feature. Due to the phase matching angle (θ_B), the Fourier plane (FP, dashed-dot line) is not in the median plane of the crystal. This limits the available aperture of the device.

100 kHz). The waveform consists of an initial Fourier-limited pulse followed in time by a replica, a linearly chirped pulse with a quadratic spectral phase, a cubic spectral phase pulse and finally a quartic spectral phase pulse.

An other example in the mid-IR is shown in figure 16 [61]. It consists of a linearly chirped pulse at 4.9 μm and its corresponding Wigner function.

Limitations. The nonlinear geometry of the $4f$-line and the nature of the interaction lead to different limitations from the LC-SLM $4f$-line. A detailed review of them can be found in [76], and is summarized here.

- Each acoustic grating pattern appears frozen during the interaction with a femtosecond pulse. As it has to be synchronized with the optical pulse, the repetition rate of the laser is limited. An optical pulse is diffracted each physical refreshing time $\Delta\tau$ of the modulator. With the

numerical values above [76], this gives a repetition rate that has to be below 100 kHz.

- The geometry of the interaction (figure 17) shows that, due to the phase matching angle θ_B, the effective optical spot size has a diameter w_{eff} which should be smaller than the minimum acoustic feature in order to maximize the resolution. Moreover, also due to this phase matching angle, the Fourier plane (FP, dashed-dot line) is not in the median plane of the crystal. To allow interactions with a good resolution, the focus of each spectral component should be included in the crystal (modulo their Rayleigh length z_R). Thus, the angle between the Fourier plane and this median axis fixes the available optical bandwidth and the acoustic frequency (equation (28)). As the acoustic bandwidth is generally proportional to the acoustic frequency, this fixes also the minimum acoustic feature and thus the achievable complexity.

- The geometry of the line also introduces dispersive effects. First, the path lengths vary significantly for different optical frequencies (longer for the blue than the red, see figure 12). This effect, which is in the first-order quadratic, has to be compensated for. A second effect is related to the Bragg angle and its dependence on optical frequencies. The mismatch is much more important for short (broadband) pulses and limits the extension of AOM pulse shaping to very short pulses.

- Finally, the absorption of the acoustic wave limits the crystal length and nonlinear effects on the acoustic waves imposes the need to work at relatively low efficiency. Moreover it is sometimes required to work in a closed-loop regime in order to compensate for this effect and to reach the desired optical waveform.

3.3.3. Other masks. In parallel with the two main spatial light modulators (LC-SLM, AOM), other masks have been developed for specific applications:

- MMDM: this micro-machined deformable mirror is commonly used for wavefront correction of nonlinear effects. It is composed of a coated membrane suspended over an array of actuator electrodes on a printed circuit board [90]. The deformation of the reflecting surface is governed by an electrostatic force. Such a MMDM mask placed in the Fourier plane of a folded $4f$-line allows smoothly varying phase-only modulation, in addition to low losses and relatively high actuator density. It represents a fairly low-cost solution which could be extended over a very broad spectral range depending on the coating of the mirror. Compression of ultrashort pulses down to 15 fs [90] as well as more complex pulses shaping [91] have been obtained.

- MEMMS: this is a micro-electro-mechanical system placed in the Fourier plane of a folded zero dispersion line. It consists of an array of independently addressable piston-type micro-mirrors, which are fabricated by surface-micro-machining. The device is activated by applying a voltage between the mirror and the address electrode, which causes the mirror to move back [92]. The choice of the coating allows high efficiency from the UV to the NIR. Compressions as well as complex pulses obtained by phase modulation have been demonstrated by several groups [92–94]. The main drawback is the appearance of strong replicas due to both pixellization and the large gaps between the mirrors.

- 2D-LC-SLM: this is a phase-only LC-SLM consisting of a matrix of pixels. The spectral components of the pulse are spread across the horizontal dimension, and a sawtooth phase function is applied along the vertical direction by the 2D LC-SLM to each frequency component [95] (the period of this function determines the direction of the first-order diffracted light). The spatial phase (i.e. vertical position) and amplitude of the sawtooth pattern can be varied for each spectral component to modulate the phase and the amplitude of the diffracted light [57]. Depending on the way the sawtooth phase function is used, a high efficiency or a superior dynamic range of modulation can be obtained [96]. Complex pulse shapes as well as simple compression have been successfully demonstrated [57, 96].

Table 2 gives an outline of the main technical characteristics of available masks presented in this section. Technical details such as control type, parameters number, efficiency, refreshing rate and damage threshold are given where available in the cited reference.

3.4. Shaping by phase transfer

The second approach to shape the amplitude and the phase of an ultrashort pulse is to perform frequency mixing between the input pulse and a control field $f(t)$ which can be either in the optical or in the acoustic domain.

3.4.1. Acousto-optic programmable dispersive filters (AOPDF). A $4f$ pulse shaper is one of the oldest and most widespread apparatus for pulse shaping. However, an alternative system has appeared in the 1990s called AOPDF or Dazzler$^{\text{TM}}$ as its commercial name (Fastlite). It is based on the acousto-optic interaction between a controlled acoustic wave $f(t)$ and an optical ultrashort pulse $E(t)$ [99, 100]. The interaction is similar to the Bragg diffraction which occurs in chirped mirrors. In the latter, the grating is permanent, fixed by the dielectric coatings. In the AOPDF, the acoustic wave creates a longitudinal transient grating which maximizes the interaction length. Practically, the acousto-optic crystal is highly birefringent for the acoustic as well as for the optical waves. In the crystal, the acoustic wave shapes by diffracting the ordinary incoming optical wave to the diffracted extraordinary optical wave. Thus, optical pulse shaping in phase and amplitude is achieved through anisotropic interaction. The change of polarization is produced by the anisotropic interaction which is different from the isotropic interaction in the AOM spatial light modulator.

As shown in figure 18, the input optical pulse is chosen to propagate along the ordinary axis (fast axis).

The different spectral components are diffracted on the extraordinary axis when the wave vectors and frequencies fulfil the phase matching condition and energy conservation:
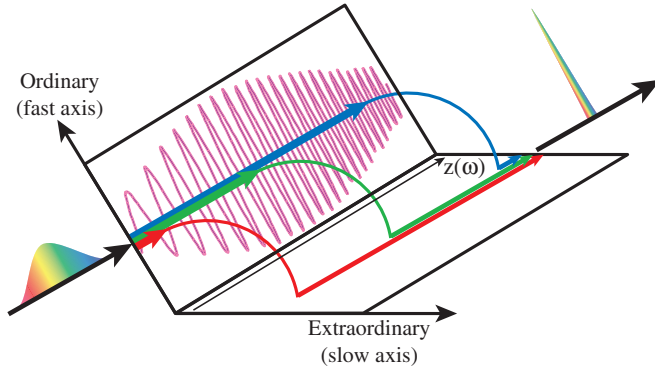
Figure 18. AOPDF principle: by diffraction on the acoustic grating through an acousto-optic interaction, the different spectral components can be switched to the extraordinary axis at different positions in the crystal.

$$\vec{k}_{\text{diff}}(\omega_{\text{diff}}) = \vec{k}_{\text{ac}}(\omega_{\text{ac}}) + \vec{k}_{\text{in}}(\omega_{\text{in}}) \tag{31}$$

$$\omega_{\text{diff}} = \omega_{\text{in}} + \omega_{\text{ac}} \simeq \omega_{\text{in}} \tag{32}$$

where 'diff' denotes the diffracted optical beam, 'in' denotes the input optical beam and 'ac' denotes the acoustic wave. This means that the spectral components can be switched to the extraordinary axis at different positions in the crystal, by changing the frequency ω_{ac} along the crystal. As the group velocities of the ordinary and extraordinary axis are different, one gets a different arrival time at the output of the crystal for each wavelengths. This time depends on the phase matching between the acoustic and the optical frequencies. Moreover the acoustic intensity at the switch location controls the amplitude of the diffracted spectral component.

The shape of the diffracted wave thus depends on both the switch position and the local acoustic intensity. One can write in the spectral domain

$$\tilde{E}_{\text{diff}}(\omega) \propto \tilde{E}_{\text{in}}(\omega) \cdot f(\gamma\omega) \tag{33}$$

or equivalently in the time domain

$$E_{\text{diff}}(t) \propto E_{\text{in}}(t) \otimes f(t/\gamma) \tag{34}$$

where the scaling factor $\gamma = \omega_{\text{ac}}/\omega \simeq (v_{\text{ac}}\delta n)/c$ ($\sim 10^{-7}$ in TeO$_2$). δn is the crystal optical anisotropy, v_{ac} the acoustic wave velocity. The factor γ allows the transfer of the acoustic waveform to the shape of the optical wave.

The shaping properties of the AOPDF have different origins from $4f$-line shapers and have to be properly defined:

- As for the other pulse shapers, it is possible to define a time window in which it is possible to shape the pulse. This window has a different physical origin than for a $4f$-line and is mainly determined by the crystal thickness and its anisotropy. The shortest programmable delay is fixed by a complete propagation along the ordinary axis while the longest delay corresponds to a propagation along the extraordinary axis. The difference between both gives the maximum time window:

$$T_{\text{max}} = \delta n_g \cos^2(\theta_{\text{in}}) \frac{L}{c} \tag{35}$$

where L is the length of the crystal and δn_g the group index difference. For a 25 mm TeO$_2$ crystal [100] this

gives $T_{\text{max}} \simeq 3$ ps at 800 nm and for a 72 mm KDP crystal $T_{\text{max}} \simeq 7$ ps at 300 nm [101]. Usually a part of this window is used to self-compensate for the dispersion due to the propagation in the acousto-optic crystal itself. This leads, in general, to an available time window of few ps.

- The resolution is given [102] by

$$\delta\lambda = \frac{0.8}{\delta n \cos^2(\theta_{\text{in}})} \frac{\lambda^2}{L} \tag{36}$$

where θ_{in} is the angle between the incident wave vector and a reference crystallographic axis. The resolution is typically equal to 0.25 nm at 800 nm and down to 0.1 nm at 266 nm for commercially available devices.

- The number of control parameters, N_{cp}, is given by the number of resolution points in the programmed diffracted bandwidth. In the case of phase-only shaping, this bandwidth has to be broad enough to diffract all the optical components with a nearly constant amplitude. Experimentally, it is set to three times the optical bandwidth, which gives

$$N_{\text{cp}} = \frac{\Delta\lambda}{\delta\lambda} = \frac{\delta n L}{0.8} \cos^2\theta_{\text{in}} \frac{3\Delta\lambda}{\lambda^2}. \tag{37}$$

For a 72 mm KDP crystal ($\theta_{\text{in}} = 48.5°$, $\delta n = 0.045$ and $\Delta\lambda = 3$ nm at 410 nm) [101], this gives $N_{\text{cp}} \simeq 100$ and around 400 in the IR [102].

- The efficiency depends on the phase matching, the length of the crystal, the merit factor of the crystal, the wavelength and finally the acoustic power. A detailed theoretical description can be found in [102].

Design and alignment. Taking into account the value of the scaling factor γ, the acoustic wave should have a frequency value around tens of MHz to allow the shaping of visible wavelength (hundreds of THz). The acoustic wave is a travelling wave synchronized with the optical wave. It is generated by a transducer glued on the crystal and monitored by a high frequency synthesizer (cf figure 19).

The crystal angle is chosen to give the best compromise between efficiency and resolution [102].

In practice, two experimental parameters are important:

- The alignment of the beam within the AOPDF has to be performed carefully. The beam has to enter the AOPDF horizontally, in the centre and normally to the inner face (auto-collimation). The best resolution is achieved when the beam is carefully collimated. The fine angular alignment of the device is made by shaping the diffracted optical beam with a thin hole in amplitude and looking at its spectrum. The corresponding spectrogram will present a hole which can be spectrally shifted by rotating the AOPDF. Once the hole is at the same wavelength as the programmed one, the phase matching condition is fulfilled and the AOPDF aligned.

- Due to the difference of speed in the crystal, the acoustic wave is seen frozen by the optical one. However, it is a travelling wave and it has to be precisely synchronized with the optical wave. To avoid any spectral clipping, the acoustic wave should be centred in the crystal when the optical waves enter in it.
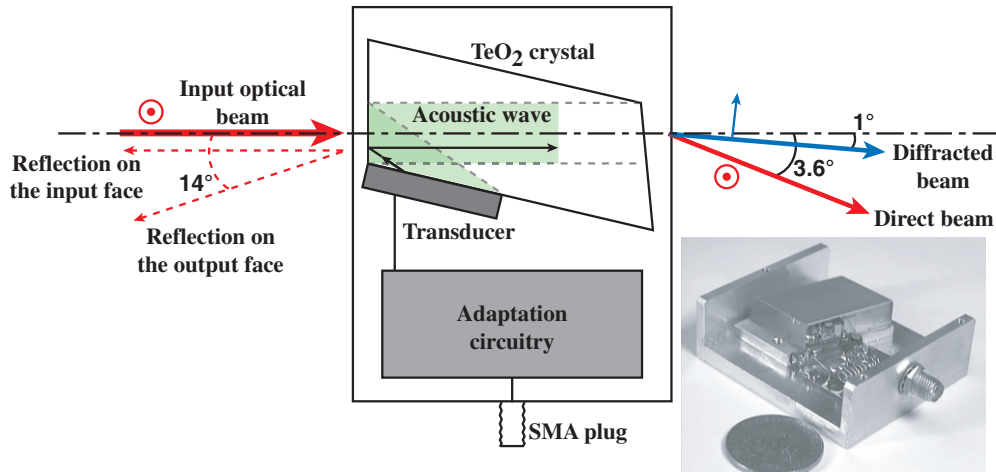
Figure 19. Experimental view of the AOPDF (courtesy of N Forget): the optical wave propagates collinearly with the acoustic waves induced by the transducer glued on the acousto-optic crystal (here TeO_2). The optical wave is diffracted on the acoustic wave and the shaped pulse goes out of the AOPDF following the diffracted beam direction. The size of the apparatus is a few cm in the IR–visible and around 10 cm in the UV.
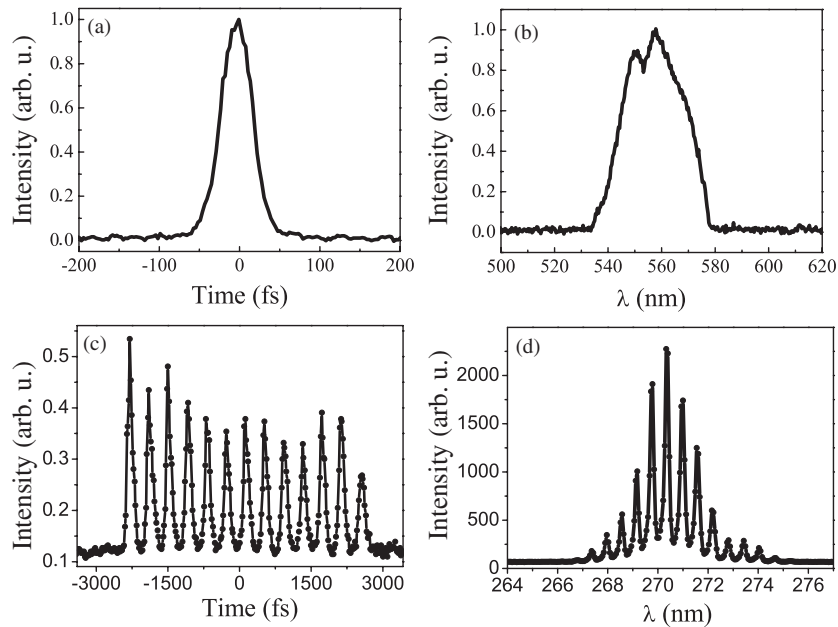

Figure 20. Results obtained with an AOPDF. In the visible range: (a) autocorrelation of the output of a NOPA compressed by the AOPDF and (b) the corresponding spectrum. In the UV range (270 nm): (c) cross-correlation of a 13-pulse sequence with a reference ultrashort pulse at 800 nm and (d) the corresponding spectrum.

Results. The AOPDF has been often used at the input of an amplifier in order to compensate for high-order dispersion leading to impressive results in the IR [103]. Intense shaped pulses have also been obtained directly at the output of a visible amplifier [104], leading to pulse duration around 30 fs (see figure 20(a): output autocorrelation, (b) output spectrum). Many other applications have been demonstrated such as high harmonic tunability [105], compression of fibre amplifier outputs [106], coherent control experiments [107]. AOPDFs are now available for wavelength ranging from 200 nm [101, 108] to 2 μm. Figures 20(c) and (d) present a 13-pulse sequence obtained at 266 nm. Improvements are under study to fabricate an AOPDF in the mid-IR [109].

Limitations

- The main limitations of the AOPDF are related to the fact that it is basically an acousto-optic modulator. For example, the travelling time of the acoustic wave in the crystal limits the repetition rate of the laser: the acoustic wave has to be refreshed for each incoming optical pulse, which limits the repetition rate to hundreds of kHz. As in an AOM 4f-line, nonlinear effects as well as absorption will also occur on the acoustic waves.
- Other limitations are strongly linked to the nature of the interaction: shaping is done by delaying the different spectral components. So on the one hand, in order to have a good efficiency in the interaction, the acoustic wave

has to be spread along the whole crystal and on the other hand, the spreading of the acoustic wave in the crystal is mainly governed by the programmed shape. This means for example that programming a strongly chirped pulse will lead to a more efficient interaction than programming a short pulse which implies that all the optical frequencies will be diffracted over a very short time [110].

- Nonlinear effects on the optical waves will be more important due to the fact that the pulse is not spatially dispersed as it is in a $4f$-line, leading to higher fluence.
- Finally, as frequency components are diffracted at different positions in the crystal, they will suffer from spatio-temporal coupling.

3.4.2. Nonlinear frequency mixing. The prospect of generating an arbitrarily shaped optical pulse has triggered significant developments in many fields of fundamental and applied research. This has led to a great effort to extend the spectral ranges where such shaped pulses are available. One way which has been detailed above is to develop pulse shapers in different spectral ranges. Another option is to use nonlinear mixing to transfer the shape of the control pulse obtained easily in the NIR range to another wavelength range. Interesting results have been obtained in the mid-IR [111, 112] as well as in the UV range [113, 114]. However, this phase transfer occurs with constraints in terms of phase matching conditions, energies and bandwidths. For example, when sum frequency mixing a control field with an independent field, the technique is linear. However, this is no longer true when generating the second harmonic of a control field. In particular, many works have demonstrated that the shape of the input pulse can completely alter the bandwidth of the SHG-generated pulse [4, 115]. As demonstrated in [116, 117], the use of two chirped pulses allows a very efficient generation of second harmonic picosecond pulses.

3.5. Conclusion on pulse shaping

This section, albeit many pages long, only shows the tip of the iceberg of pulse shaping. Before listing some achievements using different kind of pulse shapers, we would like to remind the reader of a few facts when dealing with a pulse shaper:

- The shortest feature at the output of the pulse shaper will always be governed by the available optical bandwidth.
- The maximum temporal window T will be given by the set-up as well as the optical beam properties (see section 3.2.2).
- Arbitrary pulse shapers provide a complexity η of few hundreds. This gives the ratio between the bandwidth and the minimum spectral feature available in the spectral domain or $T/\delta t$ in the time domain. Sometimes a simpler device may achieve a higher complexity (see table 1).

Finally more than hundreds of references in various fields are using pulse shapers. Table 3 presents some realizations of pulse shapers. They are sorted by shaper type and wavelength range. When available, the input pulse properties are given as well as the shaping type. Then the main results are specified.

This table does not mention all the specific references which detail the analysis and limitations of those techniques. For this information, the reader should refer to the corresponding sections above.

4. Characterization of ultrashort shaped pulses

4.1. Prerequisite and generality

When looking for a characterization technique, beginners may be puzzled by the number of available methods. Indeed, there exist a vast variety of methods, ranging from simplistic and limited to the most complex and refined one. We will not describe all of them here and interested readers are invited to read a recent review in this domain [13] and the various articles of a special issue on pulse characterization [127] for a more exhaustive overview. We will restrict ourselves to the most widely used methods, lying in three categories with increasing degree of complexity and refinement. Methods lying in the first category are said to provide *incomplete characterization* of the pulse. They usually give an estimate of the pulse duration or of the pulse intensity envelope without allowing a full reconstruction of electric field $\mathcal{E}(t)$. The most widely used methods for incomplete characterization are presented in section 4.2. The two other categories contain *referenced complete characterization* methods, and *self-referenced complete characterization* methods. All these methods allow a full reconstruction of the electric field $\mathcal{E}(t)$. The main difference between the first and the second category is that methods lying in the first one necessitate the use of a fully characterized reference pulse (see section 4.3) whereas methods in the latter category do not need any (see section 4.4).

In the following, we will equivalently refer to a pulse in the time domain by either its real electric field $\mathcal{E}(t)$ or its complex counterpart $E(t)$ as the latter usually leads to simpler equations.

4.2. Incomplete characterization methods

These methods are among the easiest to implement and are extremely widely used. However, they provide limited insight into the pulse structure but are nonetheless useful for a quick estimate of the pulse duration. The two methods we will present here are based on nonlinear correlation in a $\chi^{(2)}$ crystal, namely pulse autocorrelation and cross-correlation between two different pulses. The former is more adapted to pulses close to the Fourier transform limit whereas the latter can be used to get some insight into the time structure of a shaped pulse using an ancillary short pulse.

In the following, we will assume that the $\chi^{(2)}$ crystal used is thin enough to avoid any spectral windowing due to phase matching.

4.2.1. Autocorrelation. Autocorrelation is one of the oldest and most widely used methods to estimate the duration of a short pulse. The principle is the following: the test pulse is split into two replicas with a relative delay in a Michelson

Table 3. Table of arbitrary pulse shaping experimental demonstrations; the first column mentions the shaper type, the second column, the citation number, the third and fourth column are the main source parameters (central wavelength, duration). The shaping type can be P: phase only, P-A: phase and amplitude pulse shaping or Pol: polarization pulse shaping. Finally, in the last column, the main results of the reference are presented. NA: characteristic not available. SFM: sum frequency mixing; DFM: difference frequency mixing. SHG: second-harmonic generation. THG: third harmonic generation.

Shaper type	Ref.	Source parameter λ_0 (nm)	Source parameter Δt (fs)	Shaping type	Main results
	[97]	400 800	35 40	P	Compression of ultrashort pulses in UV and IR using LC mask
	[69]	Vis	<20	P-A	Closed-loop compression down to 16 fs from a non-collinear optical parametric amplifier (NOPA)
	[118]	Vis	NA	P-A	White-light shaping and amplification. Production of different colour pulses
	[67]	778	30	Pol	Control of two photon absorption using polarization shaping
	[60]	795	100	P-A	High-resolution (0.06 nm/pixel) phase and amplitude pulse shaper
	[119]	800	70	P-A	First use of two $4f$-line shaper for amplitude and phase control
$4f$-line + LC (pixelated)	[68]	800	13	P	Complex phase shaping of ultra-broad-bandwidth pulses
	[56]	800	80	Pol	Polarization pulse shaping
	[70]	800	20	P	Phase shaping improvement using 512 pixels
	[120]	800	30	P	Robust and flexible set-up for pulse shaping
	[121]	804	50	P	High-resolution (0.15 nm/pixel) phase shaping using 640 pixels
	[122]	800	4.3	P	Pulse shaping of octave spanning fs pulses with prisms-pulse shaper. Source: oscillator
	[123]	800	6	P	Pulse shaping of octave spanning fs pulses with prisms-pulse shaper. Source: amplifier+argon filled glass capillary fibre
	[89]	260	55		Deep UV pulse shaping using fused silica AOM
	[78]	400	100		First implementation of direct UV shaping using AOM
	[80]	400	100		Closed-loop pulse compression in the UV and optimization of CARS signal
	[98]	Vis	NA		Amplification and shaping of white light from a NOPA. 70 nm@620 nm
$4f$-line + AOM	[75]	620	180	P-A	First implementation of AOM based pulse shaping
	[81]	777	30		Closed-loop optimization of multiphoton transfer in the strong field regime
	[76]	780	90		Theoretical and experimental study of the limitations of AOM based pulse shaping
	[79]	795	150		Amplified pulse shaping (pulse shaper placed in front of the amplifier) (200 μJ)
	[61]	4900	140		Direct pulse shaping in the mid IR. Efficiency up to 30%
	[108]	270 330 404	55		Complex and tunable shaping in the UV using AOPDF with KDP crystal
	[101]	402	NA		Theory and experiments on UV AOPDF. Efficiency up to 50%
	[104]	500 − 650	30		Shaping at the output of a NOPA. Efficiency up to 50%

Table 3. (Continued.)

| Shaper type | Ref. | Source parameter | | Shaping type | Main results |
		λ_0 (nm)	Δt (fs)		
AOPDF	[107]	~570	$\Delta\lambda = 60$nm	P-A	Optimal control and enhancement of the three-photon fluorescence from molecular iodine
	[100]	800	17		First shaping using TeO$_2$ AOPDF. Compression down to 17 fs was achieved by fine phase and gain narrowing correction
	[103]	800	10		Production of terawatt scale sub-10-fs laser pulse at 1 kHz repetition rate
	[105]	810	30		Enhancement of the efficiency and tuning of the high harmonic generation using a closed loop
Phase transfer	[113]	200	155	A	Amplitude shaping at 200 nm using SFM of a shaped fundamental pulse and THG pulse
	[114]	344	19	P-A	UV shaping using SFM between a shaped NOPA pulse and a stretched IR pulse
	[124]	400	NA	POL	UV polarization shaping by SHG in two nonlinear crystals of a polarization-shaped IR pulses.
	[125]	3000–10 000	~200 fs	P	Mid IR phase shaping by DFM of the signal (1.1–1.6 μm) of an OPA and the idler
	[126]	3300	NA	P-A	Mid IR phase shaping by OPA process using shaped IR pump pulse by an AOM placed in a 4f-line
	[111]	12 000	NA	P	Phase shaping in the IR by DFM between two fundamental chirped pulses
4f-line + MEMM (pixelated)	[93]	266	100	P	Compression of deep UV broadened pulses using a closed loop
	[94]	320	30		Phase control of tunable UV pulse and two photon autocorrelation
	[92]	404	80		First shaping using MEMM. Compression and sinusoidal modulation
4f-line + MMDM	[90]	800	15	P	High-order compression down to 15.2 fs using a closed-loop approach
	[91]	842	~100	P	Precise phase control and characterization using negative feedback
2D LC (pixelated)	[95]	805	40	P-A	Amplitude and phase shaping using a phase-only 2D spatial light modulator
	[96]	800	~50	P-A	Comparison between two pulse shaping scheme in terms of efficiency and modulation

interferometer, and both replicas are focused and spatially overlapped inside a $\chi^{(2)}$ crystal. The intensity of the generated second harmonic is recorded as a function of the delay. When both replicas overlap in time inside the crystal, the second harmonic signal increases: the better the overlap, the higher the second harmonic signal. There exist two different kinds of autocorrelators: background-free intensimetric ones [128] and interferometric ones [129].

Intensimetric autocorrelator is described in figure 21: the two delayed replicas are focused in the crystal with an angle. The second harmonic generated inside the crystal contains three contributions: the upconversion of the first replica $E(t)$ with itself, the upconversion of the second replica $E(t - \tau)$ with itself and the cross-term between both replicas. Due
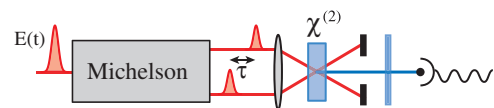
Figure 21. Intensimetric autocorrelator: the two delayed replicas are focused on the crystal with an angle and only the cross-term of the second harmonic is recorded.

to momentum conservation rules, each contribution exits the crystal in a different direction, the cross-term being on the axis. Using a spatial filter, this term is selected and sent to a slow photodiode. The electric field impinging on the photodiode can thus be written as $E_2(t, \tau) \propto E(t)E(t - \tau)$. The photodiode is assumed to be slow compared to the pulse

duration: in other words, the electrical signal it provides is proportional to the integrated intensity of $E_2(t, \tau)$:

$$S(\tau) \propto \int |E_2(t, \tau)|^2 \, \mathrm{d}t \propto \int I(t)I(t - \tau) \, \mathrm{d}t. \quad (38)$$

The intensimetric autocorrelator thus gives access to the autocorrelation function of the intensity envelope of the test pulse. It is said to be 'background-free' as the signal goes back to zero when the two replicas do not overlap in time. The main advantage of such a device is its simplicity. However, it provides limited information on the pulse itself. Indeed, to estimate a pulse duration from the autocorrelator signal, one has to make an assumption on the pulse profile [128]. Moreover, the autocorrelation function is symmetric in time, which means that a pulse preceded by a pre-pulse will give the same signal as a pulse followed by a post-pulse. This time ambiguity can be particularly limiting when trying to compensate for cubic phase terms. Finally, the intensimetric autocorrelator does not provide any information on what is below the envelope. In particular, a chirped pulse can give exactly the same autocorrelation signal as a longer Fourier-limited pulse.

The interferometric autocorrelator differs from the intensimetric one in that both replicas are collinearly focused in the crystal. In this case, the electric field impinging on the photodiode contains all the terms of the second harmonic and the signal is now

$$S(\tau) \propto \int |E(t) + E(t - \tau)|^4 \, \mathrm{d}t. \quad (39)$$

There are two main differences with the signal given by the intensimetric autocorrelator. First, even when both replicas are not temporally overlapped, the signal is not zero as it contains the upconversion signal from each replica: the interferometric autocorrelator is not background free. Second, the interferometric signal exhibits fast oscillations corresponding to the beating between the different terms in the second harmonic generation. By Fourier analysis of these oscillations, the pulse spectrum can be retrieved. An interferometric autocorrelator thus provides both an estimate of the duration and the pulse spectrum, the combination of both allowing an estimate of the time bandwidth product of the test pulse.

4.2.2. Intensimetric cross-correlation. The two autocorrelation methods presented above work well for simple pulses close to Fourier limited. However, they provide limited insight for complex pulses such as pulse sequences or strongly shaped pulses exiting from a pulse shaper. For this kind of pulses, intensimetric cross-correlation with a short pulse is better suited. As shown in figure 22, the only difference between cross-correlation and autocorrelation set-ups is that one of the two replicas of the test pulse is replaced by an ancillary short pulse.

Such a cross-correlation set-up provides us with a reconstruction of the intensity profile $I(t)$ of the test pulse, convoluted by the intensity profile of the short ancillary pulse. As an example, figure 10 shows the cross-correlation signal obtained when using a 100 fs ancillary pulse to characterize
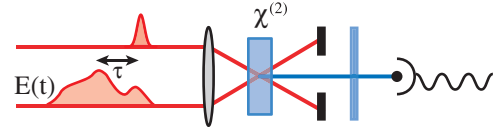

Figure 22. Cross-correlation: the test pulse $E(t)$ is non-collinearly mixed with a short one in a $\chi^{(2)}$ crystal and the sum-frequency signal is recorded as a function of the delay τ between each pulse.

different complex shaped pulse sequences. One feature of intensimetric cross-correlation is that the delay does not need to be optically stable (i.e. with a jitter lower than the optical period). Moreover, ancillary and test pulses can be in different spectral domains. The only constraint is that the ancillary pulse has to be coherent with the test pulse, and short enough to resolve its intensity structure. The main limitation is that intensimetric cross-correlation does not give any information on the phase. As an example, when characterizing a pulse sequence, the cross-correlation signal will be independent of the relative phase between the pulses in the sequence [130].

4.3. Referenced complete characterization methods

Methods presented here allow for the full reconstruction of the electric field $\mathcal{E}(t)$ of the test pulse provided a fully characterized reference pulse is available. As we have seen in section 2.1, all the information concerning an ultrashort pulse is contained in its electric field $\mathcal{E}(t)$, or equivalently in both its spectral phase $\varphi(\omega)$ and spectral amplitude $A(\omega)$. A *complete characterization* of a short pulse should thus give either $\mathcal{E}(t)$ or both $\varphi(\omega)$ and $A(\omega)$. Unfortunately, for a femtosecond pulse, a direct measurement of $\mathcal{E}(t)$ is not achievable. Indeed, it would require a detector with a time response shorter than the optical cycle of the pulse to characterize (typically few femtosecond in the visible). Such a detector does not exist and the fastest detectors exhibit time response around hundreds of femtosecond[11]. Any complete characterization method must thus provide an indirect way to access both $\varphi(\omega)$ and $A(\omega)$.

For that purpose, referenced complete characterization methods make use of a reference pulse whose spectral phase $\varphi_{\mathrm{ref}}(\omega)$ and amplitude $A_{\mathrm{ref}}(\omega)$ are perfectly known. The two main referenced techniques are spectral interferometry and Fourier transform spectroscopy. They are conceptually extremely close and completely equivalent, the only difference being that the former lies in the frequency domain whereas the latter in the temporal domain.

4.3.1. Spectral interferometry. Pioneered by Froehly and co-workers [132], spectral interferometry is based on a simple set-up that contains barely more than a spectrometer, as depicted in figure 23. The test pulse $E(t)$ and the reference pulse $E_{\mathrm{ref}}(t)$ are recombined with a delay τ and sent into a spectrometer. The complete characterization is a a two step process. First, the reference is blocked and only the test pulse is sent to the spectrometer. As one would expect, the spectrometer measures

$$I(\omega) = \left| \tilde{E}(\omega) \right|^2 = A^2(\omega) \quad (40)$$

---

[11] The only exception to date is the direct measurement of a few-cycle femtosecond pulse by sampling with an XUV attosecond pulse [131].
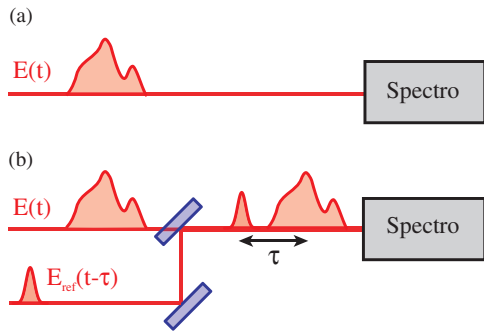
Figure 23. Spectral interferometry: the test pulse $E(t)$ is sent into a spectrometer either (a) alone to measure spectral amplitude or (b) together with a delayed reference pulse $E_{\text{ref}}(t - \tau)$ to retrieve the spectral phase.

from which the spectral amplitude of the test pulse $A(\omega)$ is directly retrieved. In the second step, both pulses are sent into the spectrometer with a fixed delay τ. The signal from the spectrometer now exhibits fringes that are due to the interference between both pulses:

$$
\begin{aligned}
I(\omega) &= \left| \tilde{E}(\omega) + \tilde{E}_{\text{ref}}(\omega)\, e^{i\omega\tau} \right|^2 \\
&= A^2(\omega) + A_{\text{ref}}^2(\omega) + 2A(\omega)A_{\text{ref}}(\omega) \\
&\quad \times \cos\left[\varphi(\omega) - \varphi_{\text{ref}}(\omega) - \omega\tau \right].
\end{aligned} \quad (41)
$$

The cosine term, responsible for the fringes, contains two contributions. The main one, $-\omega\tau$, is due to the delay and sets the overall fringe spacing. The second one, $\varphi(\omega) - \varphi_{\text{ref}}(\omega)$, encodes for the spectral phase difference between the test and reference pulses and locally modifies the fringe spacing. In other words, the interferogram can be interpreted in terms of frequency modulation: the delay acts as a carrier frequency modulated by the phase difference. The most common way to extract this phase difference from the interferogram is to use Fourier filtering [133, 134] to isolate the oscillating term and extract its argument. We first take the Fourier transform of $I(\omega)$. As depicted in figure 24, it consists of three lobes respectively centred around time $-\tau$, 0 and τ. The latter is the one containing the phase information we care about. We select this side-lobe by applying a window filter around it. Last, we Fourier transform back this side-lobe. This gives the following complex function

$$
I_\tau(\omega) = A(\omega)A_{\text{ref}}(\omega) \exp[i(\varphi(\omega) - \varphi_{\text{ref}}(\omega) - \omega\tau)] \quad (42)
$$

from which we can extract the argument:

$$
\theta(\omega) = \varphi(\omega) - \varphi_{\text{ref}}(\omega) - \omega\tau \quad (43)
$$

As $\varphi_{\text{ref}}(\omega)$ is a known quantity, we can retrieve $\varphi(\omega)$ modulo a linear phase term $-\omega\tau$. This linear term simply corresponds to a temporal delay and does not modify the shape of the test pulse. We usually remove the linear component of $\varphi(\omega)$ to centre the retrieved $\mathcal{E}(t)$ at $t = 0$.

Spectral interferometry thus provides a measurement of both $A(\omega)$ and $\varphi(\omega)$ from which the electric field $\mathcal{E}(t)$ can be

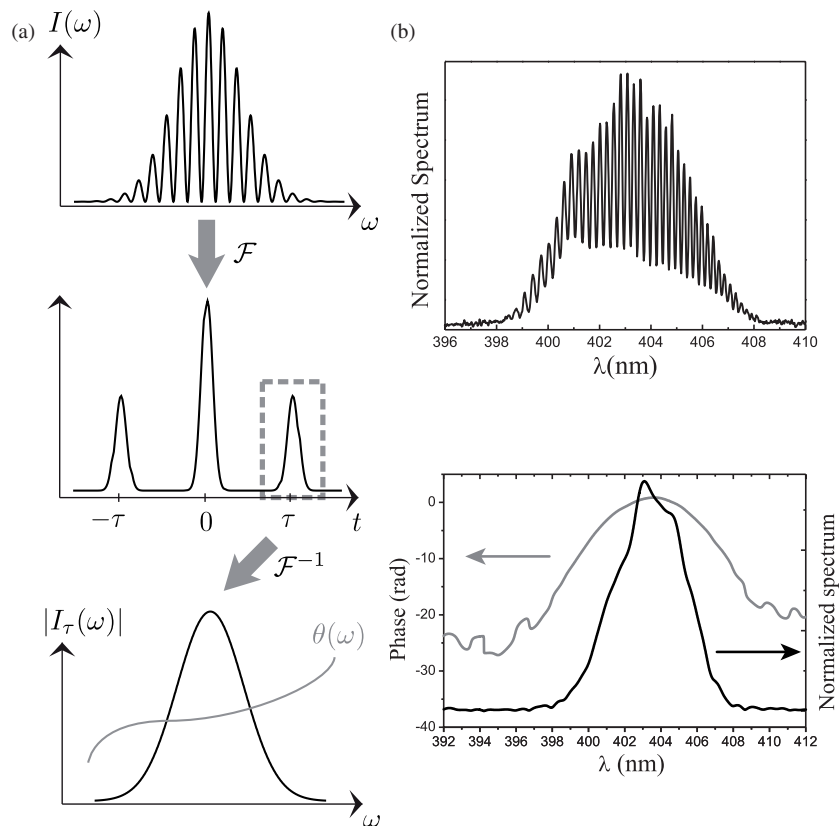**Figure 24.** Fourier filtering for spectral interferometry. (a) Principle: the interferogram is Fourier transformed and only one side lobe is kept and back Fourier transformed, giving access to the relative spectral phase $\theta(\omega)$. (b) Top: experimental interferogram using two UV pulses, one Fourier limited and one chirped. Bottom: the retrieved relative phase is in grey, the retrieved spectrum is in black.

reconstructed. However, several conditions must be fulfilled. First, in order to get interference, the test and reference pulses need to be mutually coherent (out of the same laser source). Moreover, as can be seen in equation (42), the phase can only be reconstructed where both the spectral amplitude of the test and reference pulses are non-zero. It means that the spectral amplitude of the reference pulse needs to encompass that of the test pulse. The last two conditions concern the delay τ. First, τ needs to be small enough for the fringes to be correctly sampled on the spectrometer. If $\delta\omega$ is the spectral resolution of the spectrometer, in order to get at least six points per period[12], we need to fulfil $\tau < \tau_{max} = 2\pi/(6\delta\omega)$, which sets an upperbound for τ. Second, there is also a lower bound for τ that originates from the Fourier filtering. Indeed, for it to work correctly, the three lobes at $-\tau$, 0, τ should be well separated. This implies that $\tau > 3T$, where T is the duration of the longest of both the reference and test pulse.

4.3.2. Fourier transform spectroscopy. Fourier transform spectrometry [134] contrary to its spectral counterpart does not necessitate a spectrometer. Instead, it relies on a simple photodiode whose signal is recorded as a function of a variable delay τ between two pulses. It is particularly interesting for spectral regions where spectrometers can be hard to find, e.g. in the mid-IR.

As for spectral interferometry, the retrieval of the test pulse is a two step process: the temporal interferences between two replicas of the test pulse give access to the spectral amplitude whereas the temporal interferences between reference and test pulses allow retrieving the spectral phase. As the photodiode is supposed to be slow, it acts as an integrating detector and provides a signal

$$S_A(\tau) = \int |E(t) + E(t - \tau)|^2 \, dt \qquad (44)$$

for amplitude measurement and

$$S_\varphi(\tau) = \int |E(t) + E_{ref}(t - \tau)|^2 \, dt \qquad (45)$$

for phase measurement.

In both cases, the Fourier transform of the interferogram reveals three components at $-\omega_0$, 0 and ω_0, where ω_0 is the centre frequency of the test pulse. The term at ω_0 contains all the information we need. For amplitude measurement this term gives $\tilde{E}(\omega)\tilde{E}^*(\omega) = A^2(\omega)$, which is the spectral intensity of the test pulse, whereas for phase measurement this term now reads $\tilde{E}(\omega)\tilde{E}^*_{ref}(\omega)$, whose argument is the relative phase $\theta(\omega)$ between test and reference pulses. From these two quantities and provided the reference is fully characterized, one can reconstruct the test pulse.

However, there are some constraints on the acquisition of both interferograms for this technique to work correctly: in order to avoid aliasing in the Fourier transform, the time step δt should be smaller than the optical period $t_0 = 2\pi/\omega_0$. In practice $\delta t \leqslant t_0/6$ is enough. Once the time step is fixed, the number of acquired points N set the spectral resolution $\delta\omega$ with

which both $A(\omega)$ and $\varphi(\omega)$ will be reconstructed. The needed resolution depends on the structure of the spectral phase and amplitude. For a smooth bell-shaped spectrum with a slow varying phase, a couple of tens of points across the spectrum is usually enough. Moreover, as for spectral interferometry, the reference pulse needs to be coherent with the test one and its spectrum has to encompass that of the test pulse.

4.4. Self-referenced complete characterization methods

The methods for referenced complete characterization presented above contain a huge loophole. Indeed, they rely on a fully characterized referenced pulse. Moreover, the reference pulse and the test pulse need to have similar spectral properties (central frequency, bandwidth, etc). In other words, referenced characterization methods can solve the problem of ultrashort pulse characterization provided it has already been solved once. But how do we characterize the first reference pulse?

The solution is to use a *self-referenced complete characterization technique* that does not require a reference or, in other words, that takes the test pulse as a reference for its own measurement. Methods lying in this category are the most powerful for short pulse characterization in the sense that they do not use any prior knowledge to achieve the reconstruction of the test pulse electric field $\mathcal{E}(t)$. However, this comes with a price and these methods put high requirements on the experimental set-up. In particular they require at least nonlinear or non-stationary optics. The reason for these requirements will be explained in section 4.4.1. We will then present both of the two widely used self-referenced complete characterization techniques: FROG in section 4.4.2 and SPIDER in section 4.4.3.

4.4.1. Prerequisite for self-referenced measurement of $\varphi(\omega)$. What do we need to completely characterize a test pulse $\mathcal{E}(t)$ without resorting to a reference pulse? Can we use 'usual optics', that is time-stationary linear optics? We can always try. As we have seen in section 3.1, any time-stationary linear optical set-up can be described by a complex transfer function $H(\omega)$. If we input a test pulse $\tilde{E}(\omega)$ we get as the output

$$\tilde{E}_{out}(\omega) = H(\omega)\tilde{E}(\omega). \qquad (46)$$

This set-up can be arbitrarily complex, containing many beamsplitters, interferometers or even several pulse shapers; its output can always be written as in equation (46), the complex transfer function gathering all the subtleties of the set-up. Now the best we can do is to measure the output pulse $\tilde{E}_{out}(\omega)$. For that purpose, we do not have a lot of possible detectors: either slow photodiodes or spectrometers can be used. We will continue our discussion using a spectrometer but the same conclusion can be drawn using a photodiode. The spectrometer gives access to the spectral intensity

$$I_{out}(\omega) = |\tilde{E}_{out}(\omega)|^2 = |H(\omega)|^2|\tilde{E}(\omega)|^2 = |H(\omega)|^2 A^2(\omega). \qquad (47)$$

As we can see, all the information on the spectral phase $\varphi(\omega)$ has disappeared from the expression of the signal we

---

[12] In theory, the Shannon criterion says that three points are enough. In practice, we recommend six points.
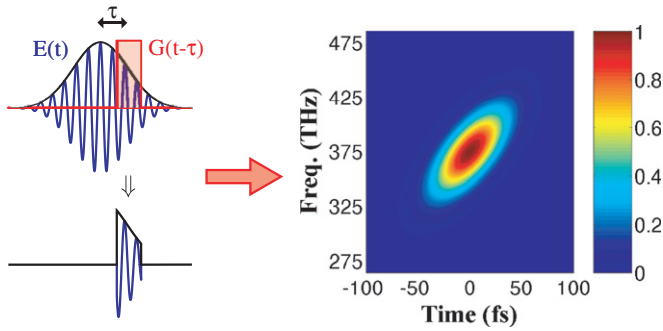
Figure 25. Principle of frequency optical gating: the test pulse $E(t)$ is temporally sliced (or gated). The spectrum of this gated pulse is measured as a function of the delay τ between the gate $G(t)$ and the test pulse.
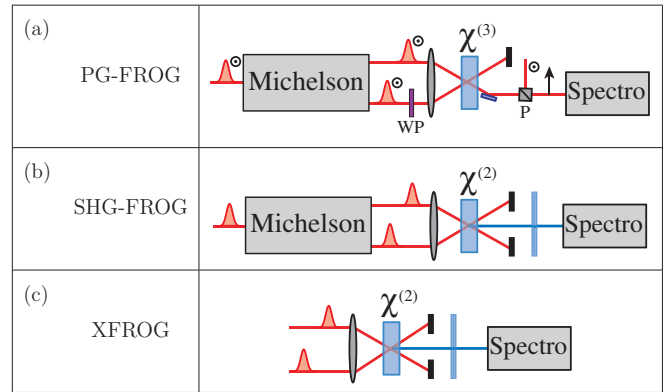

Figure 26. Schematic set-up of various versions of FROG techniques. (a) Polarization gating FROG, (b) second harmonic generation FROG and (c) cross-correlation FROG. WP is a wave plate to tune the polarization, P is a polarizer, $\chi^{(2)}$ and $\chi^{(3)}$, nonlinear susceptibilities.

measure. The only information on the pulse we can gain from this type of measurement concerns the spectral amplitude $A(\omega)$. This explains what we have seen in section 4.3 on referenced measurements: the reference was not needed to measure the spectral amplitude but was necessary to retrieve the spectral phase using linear optics. In conclusion of this quick try, the spectral phase of a short pulse cannot be measured using stationary linear optics, unless we use a fully characterized reference [135]. We thus need to use nonlinear or non-stationary optics to achieve self-referenced complete characterization of a short pulse. This is a necessary but not sufficient condition to get a complete measurement[13].

4.4.2. FROG and other variants. The oldest established technique for self-referenced complete characterization is called frequency-resolved optical gating, or FROG [25, 136]. The main idea in FROG is to temporally slice (or gate) the test pulse $E(t)$ and measure the spectrum of this gated pulse as a function of the delay τ between the gate $G(t)$ and the test pulse, as depicted in figure 25.

This gives a 2D signal,

$$S(\tau, \omega) \propto \left| \int E(t) G(t - \tau)\, e^{i\omega t}\, dt \right|^2, \qquad (48)$$

that corresponds to a spectrogram of the test pulse (see equation (8) in section 2.2). From this 2D map, one can extract the spectral phase and amplitude of the test pulse using an iterative algorithm [136–138]. It is worth noting that extracting the pulse information from $S(\tau, \omega)$ corresponds to the well-known *2D phase retrieval problem* that can be found in many different fields. Moreover, the complete characterization of the test pulse remains possible even if the gate $G(t)$ is not fully characterized or even completely uncharacterized. There exist various implementations of FROG and they mostly differ by the way the gate $G(t)$ is generated. What all these implementations have in common is that they always require a nonlinear interaction to generate the gate.

[13] In particular, both autocorrelation and cross-correlation contain a nonlinear crystal without allowing a complete measurement of the test pulse.

PG-FROG. One of the very first implementations was the polarization gating (PG)-FROG [137] where the gating is implemented using the interaction between two copies of the test pulse $E(t)$ in a $\chi^{(3)}$ medium, as shown in figure 26(a). In this particular implementation, a Kerr optical-gate is used and it results in a gate function following the intensity profile of the pulse $G(t) = |E(t)|^2$. With PG-FROG and for a reasonably simple test pulse, $S(\tau, \omega)$ is a fairly intuitive spectrogram. Some key features from the test pulse (such as for example the presence of chirp and its sign) can thus be grasped directly by looking at $S(\tau, \omega)$ without resorting to the iterative algorithm.

SHG-FROG. The most widely used FROG implementation is the second harmonic generation (SHG)-FROG [139] and its derivatives [137, 140]. One of the most widespread SHG-FROG is the so-called GRENOUILLE [140], a single-shot spectrally resolved autocorrelation. As depicted in figure 26(b), it is more easily implemented than PG-FROG as it is just an intensimetric autocorrelator where the photodiode has been replaced by a spectrometer. Now, the gate is just a time-delayed replica of the test pulse $G(t - \tau) = E(t - \tau)$ and the signal reads

$$S(\tau, \omega) \propto \left| \int E(t) E(t - \tau)\, e^{i\omega t}\, dt \right|^2. \qquad (49)$$

Although easier to implement than PG-FROG, SHG-based FROG presents two disadvantages. First, the 2D signal is not as intuitive as the PG-FROG one. Second, as can be seen in equation (49), this signal is symmetric in time which means that there is a time ambiguity and the algorithm can retrieve either $E(t)$ or $E(-t)$. One should keep this in mind when trying to compensate for chirp or to get rid of pre- or post-pulses.

XFROG. The last FROG implementation we will present here is the so-called XFROG [141] combined with the fast iterative algorithm called PCGPA [138]. This combination is particularly suited for the characterization of strongly shaped pulses or for the simultaneous characterization of pump and
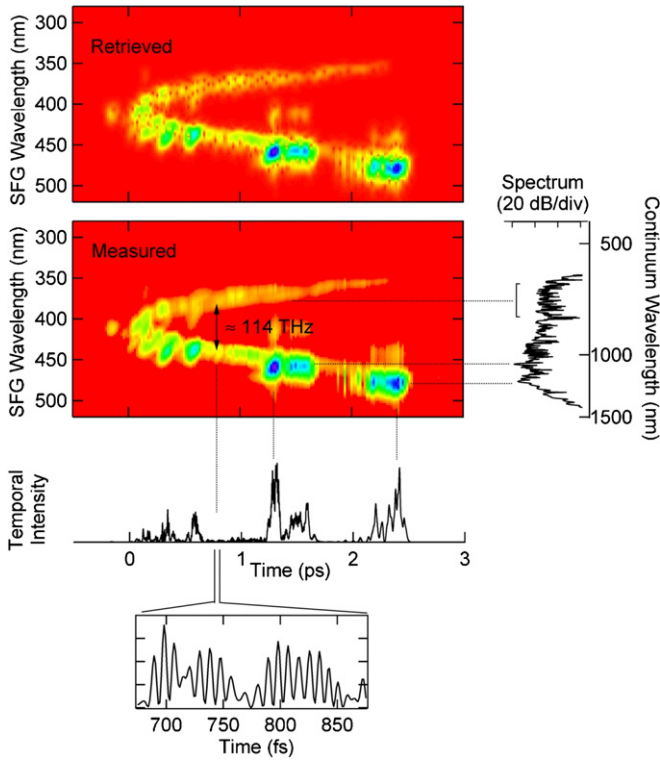
Figure 27. Taken from [144]: referenced XFROG trace and retrieved temporal intensity of a supercontinuum out of microstructured fibre using the input of the fibre as a reference.

probe pulses in coherent control experiments. XFROG is a spectrally resolved cross-correlation between two pulses, as shown in figure 26(c). Its signal takes the form

$$S(\tau, \omega) \propto \left| \int E(t) E_G(t - \tau)\, e^{i\omega t}\, dt \right|^2 \qquad (50)$$

where E_G denotes the gate pulse. XFROG thus possesses all the advantages of intensimetric cross-correlation: interferometric stability is not required for the delay between pulses and both pulses can lie in different spectral regions. It also has the ability to fully characterize both test and gate pulses simultaneously when used with PCGPA [138].

Moreover, if the gate pulse $E_G(t)$ is short compared to the test pulse $E(t)$, the signal $S(\tau, \omega)$ is an extremely intuitive spectrogram of the test pulse (see figure 3). XFROG is particularly suited to characterize the output of a pulse shaper, using a portion of the input pulse as the gate pulse. However, in many cases, XFROG is also used as a referenced measurement [142, 143] by using a fully characterized gate pulse, as it leads to better convergence of the retrieval algorithm. This can be useful to characterize the output of a microstructured fibre, as shown in figure 27.

Even when used as a referenced measurement, XFROG suffers from the same limitation as the cross-correlation: it cannot retrieve the relative phase of non-overlapping pulses of a pulse sequence.

Closing words on FROG. FROG is a powerful technique for self-referenced complete characterization of ultrashort pulses. Many variants of FROG exist [25, 136–138, 140, 141, 145,

146] (see also table 1 in [12]). Table 4 lists some achievements using various variants of FROG. Some of these variants give an intuitive signal that trained user can partially interpret without recurring to an iterative algorithm. Moreover, FROG devices are relatively easy to implement and existing set-ups (such as an autocorrelator or a cross-correlator) can be adapted to measure FROG traces.

The main drawback of FROG lies in the 2D nature of the signal and the iterative algorithm used to analyse it. First, the sampling and the covered range for both time and frequency axes have to be carefully chosen in order to reconstruct the test pulse with a good fidelity. In particular, as time and frequency are conjugate variables, the settings are not independent. Second, as all the information concerning both spectral phase and amplitude is encoded in the slow variation in intensity of $S(\tau, \omega)$, the camera used for recording the signal should exhibit both a high dynamic range and a high linearity. Finally, the number of data points to record and analyse grows quadratically with the pulse complexity η. It means that for complex pulses, the time needed for the iterative algorithm to converge increases dramatically.

4.4.3. SPIDER and other variants. There exists another method for self-referenced complete characterization that was developed a decade ago: spectral phase interferometry for direct electric-field reconstruction, or SPIDER [153] for short. We will present here the basic idea behind this technique along with some of its incarnations. This is by no means an exhaustive review, and for more details on all the different versions of SPIDER, interested readers should look at [154] and references therein. As its name suggests, SPIDER is based on spectral interferometry, with a special trick to allow for a self-referenced measurement. As we have described in section 4.3.1, when we apply spectral interferometry to a test pulse $E(t)$, using a reference $E_{ref}(t - \tau)$, we retrieve both the spectral amplitude $A(\omega)$ of the test pulse and the quantity $\theta(\omega) = \varphi(\omega) - \varphi_{ref}(\omega) - \omega\tau$ (see equation (43)) which is the phase difference between the test and reference pulses, modulo a linear term $-\omega\tau$ corresponding to the delay between the pulses.

The trick in SPIDER which turns spectral interferometry (by essence a referenced measurement) into a self-referenced measurement, is to use the test pulse itself as a reference. More precisely, we use as a reference a copy of the test pulse that is shifted both temporally and spectrally so that spectral interferometry now yields both $A(\omega)$ and

$$\theta(\omega) = \varphi(\omega) - \varphi(\omega - \Omega) - \omega\tau \qquad (51)$$

where Ω is the spectral shift (or spectral shear) and τ is the temporal shift. If τ and Ω are known, we can derive from equation (51) the following quantity:

$$\frac{\varphi(\omega) - \varphi(\omega - \Omega)}{\Omega} \approx \frac{\partial \varphi}{\partial \omega}, \qquad (52)$$

which is the phase gradient of the test pulse. From this gradient, we can reconstruct the phase either by concatenation or integration. The retrieved phase is the spectral phase of the test pulse, modulo a linear term: as already pointed out in section 2.1, this linear phase just corresponds to a delay and

Table 4. List of some of the experimental achievements using variants of FROG: for the test pulse λ_0 is the central wavelength, Δt is the duration, $\Delta\lambda$ is the spectral bandwidth, E is the smallest energy per pulse and P is the smallest average power.

Method name	Ref	Source parameter			Main characteristics
		λ_0 (nm)	Δt (fs)/$\Delta\lambda$ (nm)	E (nJ)/P (μW)	
THG $-$ FROG	[145]	800	$\simeq$100/NA	$3/3 \times 10^5$	FROG using surface THG. No time reversal ambiguity
PG $-$ FROG	[137]	620	$\simeq$100/NA	$\simeq 10^4$/NA	Original FROG using third-order nonlinearity for polarization gating. Intuitive trace, but requires energetic pulses
SD-FROG	[136]	620	$\simeq$100/NA	$\simeq 10^4$/NA	FROG using self-diffraction as a nonlinear step
	[139]	800	$\simeq$70/24	NA/NA	
SHG-FROG	[147]	800	$\simeq$90/NA	2/NA	Spectrally resolved second-order non-collinear autocorrelation. Easy to set up but time reversal and relative phase ambiguities
	[148]	1550	$\simeq$40/150	NA/5×10^3	
	[149]	5000	$\simeq$700/NA	100/NA	
IFROG	[150]	800	7/300	NA/NA	SHG-FROG but in collinear arrangement. No blurring of the FROG trace but fringes have to be resolved
GRENOUILLE	[140]	800	$\simeq$100/$\simeq$20	NA/NA	Simplified SHG-FROG using bi-prism and thick SHG crystal. Time reversal ambiguity
XFROG	[141]	4000	NA/$\simeq$100	NA/10^3	Spectrally resolved cross-correlation between two unknown pulses. Each pulse can be in different spectral regions. Both pulses are retrieved
Referenced XFROG	[143]	3000 to 11 000	$\simeq$100/$\simeq$200	$\simeq 3 \times 10^3$/NA	XFROG with one unknown mid-IR pulse and a fully referenced IR pulse. A reference is needed
	[142]	400	$\simeq$170/NA	$\simeq 6 \times 10^{-2}$/NA	XFROG using down conversion between one unknown UV pulse and a fully referenced IR pulse. A reference is needed
TG-FROG	[151]	426	$\simeq$250/$\simeq$1.5	200/200	FROG using transient grating. Adapted to UV pulses
	[152]	400	130/2.5	$85 \times 10^3/85 \times 10^3$	FROG using transient grating and a simplified set-up like GRENOUILLE
	[152]	800	150/8	$5 \times 10^5/5 \times 10^5$	

does not affect the shape of the pulse (that only depends on nonlinear phase terms). SPIDER thus allows retrieving the spectral phase $\varphi(\omega)$ of the test pulse together with its spectral amplitude $A(\omega)$ using only a simple, non-iterative algorithm: Fourier filtering to extract $\theta(\omega)$ and additions, multiplications and integration to derive $\varphi(\omega)$.

The conditions to fulfil for a meaningful measurement concern both the temporal shift τ and spectral shear Ω. The conditions for τ are exactly the same as for spectral interferometry, as described in section 4.3.1: τ should be small enough for the spectral fringes to be correctly sampled by the spectrometer and yet longer than the duration of the pulse for the Fourier filtering to work. The spectral shear Ω should be small enough to fulfil the Whittaker Shannon theorem, or in other words, to ensure that the sampling of $\varphi(\omega)$ is small enough so that no information was lost in the process. In theory any shear that respects $\Omega \leqslant 2\pi/T$, where T is the time interval where the pulse is non-zero, will produce an exact reconstruction of the spectral phase and amplitude. However,

Ω should not be too small to avoid introducing unwanted noise in the concatenation process. In practice, a shear Ω in the order of a tenth of the spectral bandwidth of the pulse works well enough.

So far we have not explained how the spectral shear Ω is generated. This is where a nonlinear or non-stationary stage is involved. Indeed, as shown in figure 28(a), the sum frequency mixing between our test pulse $\tilde{E}(\omega)$ and a quasi-monochromatic beam of centre frequency ω_1 gives $\tilde{E}(\omega - \omega_1)$, which is a spectrally shifted copy of the test pulse. In practice however, this introduces a spectral shift that is two to three orders of magnitude too high for SPIDER and that is not easily tunable. To circumvent this problem, the set-up presented in figure 28(b) is used: all time-delayed replicas of the test pulse $E(t)$ and $E(t - \tau)$ are sum frequency mixed in a nonlinear crystal with a highly chirped pulse $E_C(t)$. This chirped pulse acts as a quasi-monochromatic pulse whose frequency changes slightly over time τ: $\omega_C(t) = \omega_1 + t/\varphi_0^{(2)}$. Each delayed replica is thus shifted in frequency by a different amount
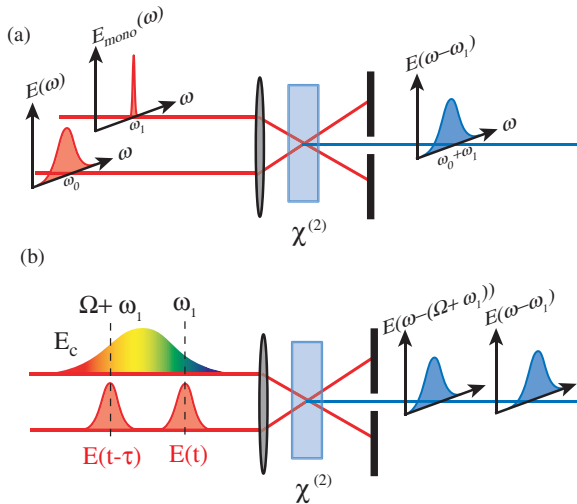
Figure 28. Spectral shearing by upconversion: (a) the upconversion between $E(\omega)$ a quasi-monochromatic pulse $E_{mono}(\omega)$ centred around ω_1 generates a spectrally shifted replica $E(\omega - \omega_1)$; (b) the upconversion between two delayed replicas $E(t)$ and $E(t - \tau)$ and a chirped pulse $E_c(t)$ leads to two delayed and spectrally shifted replicas.
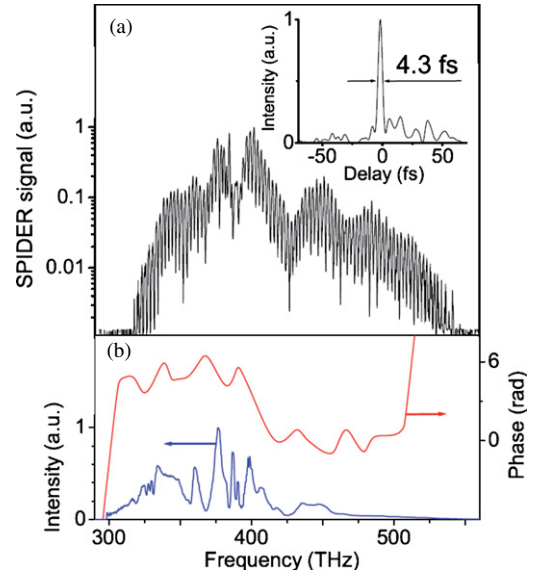

Figure 29. Different SPIDER techniques and their schematic set-ups. (a) Original SPIDER, (b) zero additional phase SPIDER and (c) spatially encoded arrangement SPIDER. $\chi^{(2)}$ denotes the nonlinear susceptibility.

and the difference in frequency shift is $\Omega = \tau / \varphi_0^{(2)}$. By adjusting independently the chirp $\varphi_0^{(2)}$ and the delay τ between the replicas, one can set both Ω and τ.

The original flavour of SPIDER. The original set-up for SPIDER is depicted in figure 29(a). The test pulse is split into two time-delayed replicas in a Michelson interferometer, which are upconverted with a highly chirped pulse in a nonlinear crystal. The upconversion signal is then sent into the spectrometer and the spectral amplitude and phase are extracted from the interferogram using Fourier filtering. Usually, the highly chirped pulse is generated from the test pulse itself by taking a fraction of it and sending it through a double pass grating compressor. However, any chirped pulse that is coherent with the test one may suffice. As an example, for weak pulses, a modified version of SPIDER (M-SPIDER) was developed [155] where the chirped pulse is taken inside

Figure 30. Taken from [156]: high dynamic range SPIDER measurement of a 4.3 fs pulse out of a fibre compressor. (a) SPIDER interferogram, (b) reconstructed spectral phase and amplitude; inset: temporal intensity profile.
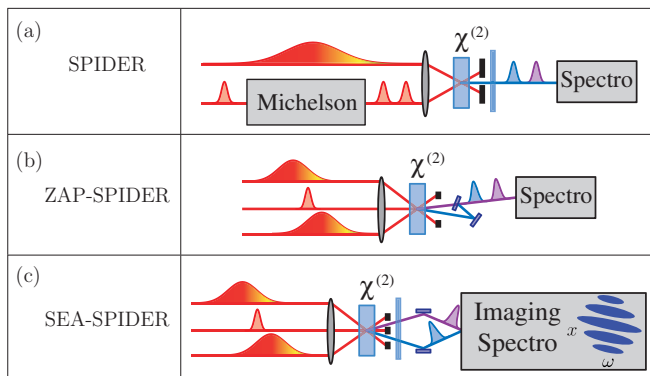
the chirped pulse amplifier before recompression. This highly intense chirped pulse increases greatly the signal-to-noise ratio.

The original version of SPIDER is relatively simple and works well for pulses longer than few tens of femtosecond. The problem for shorter pulses arises from splitting the test pulse into two delayed replicas. Indeed, this implies going through some dispersive optics, like a beam splitter, which introduces unwanted dispersion. If the two replicas do not experience the exactly same dispersion, the SPIDER measurement is degraded. However, using an optimized set-up for SPIDER [156], broadband pulses can be characterized by SPIDER, as shown in figure 30.

Two different evolutions of SPIDER have been developed more specifically to characterize broadband and complex pulses. The first one, that we will not describe here, is Homodyne Optical Technique for SPIDER (HOT SPIDER) [157] which relies on a two-step measurement and is particularly suitable for short and weak pulses. The second approach is the zero additional phase SPIDER (ZAP SPIDER) [158] which is described below.

Zero additional phase SPIDER. As its name suggests, in zero additional phase SPIDER [158], the test pulse does not experience any distortion before entering the nonlinear crystal. The untouched test pulse is upconverted with two time-delayed replicas of a strongly chirped pulse, as shown in figure 29(b). Because of the delay τ_c between the two chirped replicas, they exhibit different instantaneous frequencies when being upconverted with the test pulse. As a result, two spectrally sheared replicas of the test pulse are generated. However, contrary to conventional SPIDER, these replicas are perfectly synchronized in time as they come from the very same test pulse. Moreover, as the two chirped pulses enter the crystal with different angles, the two sheared replicas propagate in

different directions. The delay τ is independently set when recombining the sheared replicas before sending them into the spectrometer. The interferogram is similar to that of conventional SPIDER and the same analytical processing is performed. Besides the clear advantage of the introduction of virtually no distortion on the test pulse, another advantage of this arrangement is that the temporal delay τ and the shear Ω are completely independent: the former is set by delaying one of the upconverted replica before recombination whereas the latter can be set by changing the delay τ_c between the two chirped pulses. ZAP SPIDER has proved to be particularly efficient for shaped and weak pulses [159].

Spatial encoded arrangement for SPIDER. All the flavours of SPIDER we have presented so far share in common the use of spectral fringes to encode the phase gradient. However, this is not the only option and the phase gradient can also be encoded in time. This is the case in time domain interferometry for SPIDER (no funny acronym here!) [160, 161] that was developed for spectral regions where spectrometers are not easily available.

Another possibility is to encode the phase gradient in spatial fringes. This is the essence of the spatially encoded arrangement for SPIDER or SEA-SPIDER [162], particularly suited for broadband and shaped pulses. As one can see in figure 29(c), the SEA-SPIDER set-up is close to the ZAP SPIDER we just presented. The main difference is that the two spectrally sheared replicas are kept synchronized in time and are recombined, with an angle, into an imaging spectrometer. This angle produces an ensemble of fringes along the vertical axis of the CCD (the wavelength being dispersed along the horizontal axis). More precisely, for a test pulse of the form $\tilde{E}(x, \omega)$ (where x denotes the vertical coordinate), a spectral shear of Ω, and for a difference between the transverse component of the propagation vectors K, one gets the following 2D interferogram:

$$I(x, \omega) = |\tilde{E}(x, \omega)|^2 + |\tilde{E}(x, \omega - \Omega)|^2$$
$$+ 2|\tilde{E}(x, \omega)||\tilde{E}(x, \omega - \Omega)|$$
$$\times \cos[\varphi(x, \omega) - \varphi(x, \omega - \Omega) + Kx]. \quad (53)$$

The retrieval of the phase gradient is a slight modification of the conventional SPIDER algorithm: the 2D Fourier transform of $I(x, \omega)$ is composed of three lobes, all aligned along time 0 and centred around $+K$, 0 and $-K$. By filtering of the $+K$ sidelobe and inverse Fourier transforming, one gets

$$\theta(x, \omega) = \varphi(x, \omega) - \varphi(x, \omega - \Omega) + Kx \quad (54)$$

from which one can retrieve $\varphi(x, \omega)$ by concatenation, provided K is fully known. For a correct reconstruction, the conditions on the spectral shear Ω are the same as for conventional SPIDER, and the incidence difference K is set so that there are few fringes across the beam (three fringes being a minimum). An imaging spectrometer with 128 pixels across the vertical axis is more than enough to properly sample the spatial fringes.

So SEA-SPIDER works in a similar way as the normal SPIDER, but what are the advantages of this approach? First, SEA-SPIDER possesses the same properties as ZAP-SPIDER. Moreover, as the fringes are not encoded along the
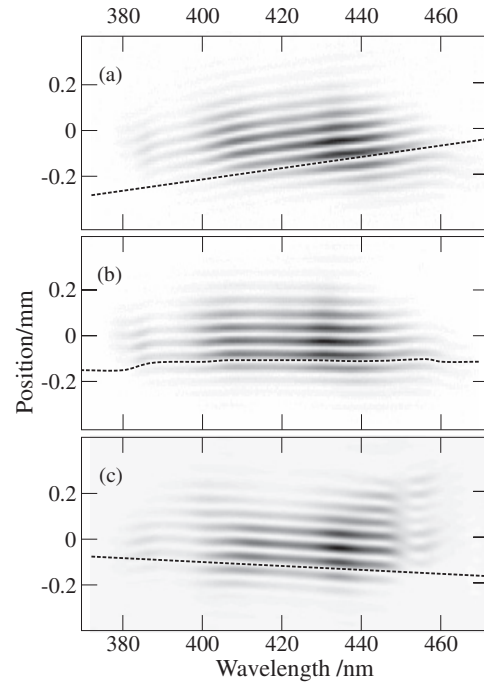

Figure 31. SEA SPIDER intuitive traces (courtesy of A Wyatt): SEA SPIDER traces for a femtolaser rainbow oscillator, (a) for a positive $\varphi_0^{(2)}$, (b) for a recompressed pulse and (c) for a negative chirp. The small wiggles in (b) are a signature of small remaining high-order phase.

frequency axis, the requirement on the spectral resolution of the spectrometer is less stringent. Indeed, in conventional SPIDER the spectral resolution has to be at least three times better than the minimum required to fulfil the Whittaker Shannon theorem. This high requirement on resolution is difficult to fulfil when dealing with extremely broadband pulses whose spectrum can span across several hundreds of nanometers. With SEA-SPIDER, the retrieval can be done at the sampling limit. SEA-SPIDER is thus the best SPIDER for shaped and broadband pulses.

The second advantage of SEA-SPIDER is that the spectral phase and the spectral amplitude are reconstructed for every position x along the vertical axis. This means that one can precisely measure spatio-temporal couplings such as spatial chirp and pulse-front tilt or even more complex distortions. This is particularly useful for broadband or shaped pulses that often exhibit this kind of distortions.

The last advantage of SEA-SPIDER over other variants of SPIDER is that the raw interferogram is intuitive: any deviation from perfectly straight horizontal fringes can be easily interpreted, as one can see in figure 31: a tilt corresponds to a $\varphi_0^{(2)}$ (figures 31(a) and (c)), a curvature to a $\varphi_0^{(3)}$, and any high-order phase translates into deviation from straight lines (figure 31(b)).

Closing word on SPIDER. SPIDER is a reliable method for measuring short and complex pulses. It comes in many flavours and the most up-to-date and exhaustive list can be found in references of [154]. Some experimental achievements using SPIDER and its variants are listed in table 5.

Table 5. List of some of the experimental achievements using variants of SPIDER: for the test pulse λ_0 is the central wavelength, Δt the duration, $\Delta\lambda$ the spectral bandwidth, E the smallest energy per pulse, P the smallest average power.

Method name	Ref	Source parameter			Main characteristics
		λ_0 (nm)	Δt (fs)/$\Delta\lambda$ (nm)	E (nJ)/P (μW)	
SPIDER	[153]	800	$\simeq$100/NA	few/few 10^5	Original SPIDER. Algebraic, non-iterative reconstruction algorithm to retrieve the phase gradient
	[166]	800	$\simeq$6/300	3/3 $\times 10^5$	
	[167]	800	$\simeq$100/NA	NA/NA	Single shot SPIDER, with simultaneous and independent measurements of spectral amplitude and spectral amplitude
	[168]	650	$\simeq$4/500	NA/NA	SPIDER optimized for broadband pulses
High Dynamic Range SPIDER	[156]	850	$\simeq$4.3/480	2×10^4/2×10^4	SPIDER using heterodyne detection based on chopper and fast 1-line CCD camera. Designed for octave spanning
HOTSPIDER	[157]	800	$\simeq$100/NA	250/250	Two-step measurement using intense auxiliary pulse. Designed for low average power/low intensity pulses
MSPIDER	[155]	800	$\simeq$100/NA	3.6/3.6	Original SPIDER but using an intense auxiliary pulse from a chirped pulse amplifier. Designed for low average power like fibre output
SPIDER (DC)	[169]	410	$\simeq$140/4	70/70	SPIDER using down-conversion as a nonlinear step. Designed for UV pulses
Time-domain HOT SPIDER	[160]	800	$\simeq$100/NA	NA/NA	HOT SPIDER in time domain using a shaper and a two-photon detector. Compact, simple set-up without spectrometer
	[161]	9200	$\simeq$150/NA	2×10^3/2×10^3	HOT SPIDER in time domain for Mid-IR pulses. No spectrometer required, designed for Mid-IR pulses
Electro $-$ Optic SPIDER	[170]	1540	750 to 30000/NA	$< 10^3$/NA	SPIDER using non-stationary step (fast electro-optic phase modulation) instead of nonlinear step. Ultra-sensitive, for telecom wavelengths
	[171]	1570	200/NA	5×10^3/NA	
ZAP SPIDER	[158]	600	10/120	NA/NA	SPIDER without splitting of the test pulse, using two auxiliary chirped pulses. Designed for short pulses ($<$20 fs)
	[159]	290	19/$\simeq$10	10/10	ZAP SPIDER using down conversion. Designed for short UV pulses
	[159]	290	7/40	10/10	
	[172]	5100	100/400	10^3/10^3	ZAP SPIDER for mid-IR pulses
HH SPIDER	[173]	73	13/8	NA/NA	High harmonic SPIDER using a double seed scheme in high harmonic generation. Designed for XUV high harmonics
SEA SPIDER	[162]	800	100/NA	10/few 10^5	ZAP SPIDER but using spatial fringes. Requires an imaging spectrometer. Designed for ultra-broadband, modulated pulses with spatiotemporal coupling
	[174]	850	7/200	$\simeq 4$/$\simeq 3 \times 10^5$	
ARAIGNEE	[175]	740 to 900	70/NA	NA/$\simeq 10^3$	Simplified set-up using a thick SHG crystal for spectral shearing
TEA SPIDER (2DSI)	[176]	800	5/400	2/2 $\times 10^5$	SPIDER but using temporal fringes to encode phase gradient

The two main advantages of SPIDER compared to competing techniques are, first, that it relies on a 1D signal and second that the phase retrieval algorithm is analytical and non-iterative. A 1D signal means that the amount of data to collect and treat is extremely small. Moreover, when using a 2D detector, like in an imaging spectrometer, one has an extra degree of freedom to play with. In SEA-SPIDER [162] for example, this allows for a simultaneous measurement of the spatio-temporal coupling. The non-iterative Fourier transform algorithm allows for true real time retrieval of the spectral phase.

One strength of SPIDER is the encoding of the phase in fringes which allows for a good reconstruction of the phase even with a poor dynamic range of the CCD (down to 1 bit) and in the presence of strong noise [155].

The main drawback in SPIDER is that the calibration is particularly crucial and should not be overlooked. However, a new version of SPIDER [163] (chirped arrangement for SPIDER, CAR-SPIDER), uses the extra dimension to encode several configurations and provides a truly calibration-free measurement. Another limitation in SPIDER is the Fourier filtering technique (also known as the Takeda algorithm [133]) that is commonly used to extract the phase gradient from the interferogram. This filtering can be tricky to set and is the limiting factor in terms of acceptable noise level for phase retrieval. A new algorithm based on fast wavelet analysis has recently been developed which addresses these two issues [164, 165].

4.4.4. Conclusion on characterization. Many different characterization techniques are available, adapted to different pulse durations and wavelengths. They range from the most simple and limited to the more refined and complex ones. Implementing at least one complete characterization method is almost compulsory when using short and sometimes shaped pulses. However, incomplete and simple methods such as auto- and cross-correlations should not be disregarded as they are easy to set up, fast and simple to use for daily check, and also provide an independent measurement. Moreover, these methods are still actively developed and extended (see for example [94]). Concerning self-referenced techniques, we only presented here a small selection and tables 4 and 5 give some more details about other variants of both FROG and SPIDER.

As a conclusion on characterization of ultrashort pulses, we would like to give a personal view on the specific problem of characterizing strongly shaped pulses out of a pulse shaper. Theses pulses, because of their complexity (or high time bandwidth product) can easily go beyond the limits of any given method. In particular, characterizing them with a self-referencing method (FROG, SPIDER or any variant of both) can be particularly difficult, requires special care and an optimized version of the method chosen for the task. Moreover, in order to properly and accurately generate this shaped output, the input pulse of the pulse shaper has to be decently characterized. For all these reasons, we believe that the most efficient approach is to combine a self-referenced measurement of the input pulse and a referenced measurement
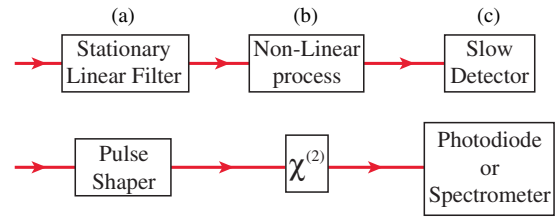

Figure 32. Generic set-up for complete characterization: (a) a pulse shaper serves as a generic versatile linear filter, followed by (b) a nonlinear process whose output is monitored by (c) a slow detector.

of the output, using the input as a reference. As the input pulse is usually not really complex, any basic variant of FROG or SPIDER can be use for its measurement. For the referenced measurement, spectral interferometry or referenced XFROG are particularly well suited and easy to set up.

5. The combination of pulse shaping and characterization techniques

The last point we would like to mention in this tutorial is the recent development of characterization techniques that directly rely on a pulse shaper, an approach we decided to call 'shaper-assisted characterization'.

One early precursor in this domain is STRUT (spectrally and temporally resolved up-conversion techniques) [177] where a $4f$ pulse shaper with a fixed slit is used to produce a spectrally narrowed replica of the test pulse (see [177, 178] for more details on the technique itself). However, in STRUT, the pulse shaper is not programmable and plays less of a central role than in more recent implementations.

The key idea behind this approach is that most pulse shapers can be turned into versatile characterization devices by simply adding few optical elements that are usually already present in the lab. Indeed, a complete characterization technique can be implemented by combining three key ingredients: a linear stationary filter, a nonlinear optical process, and a slow detector as sketched in figure 32. In shaper-assisted characterization techniques, a pulse shaper is used in order to implement the linear stationary filter with the rest of the set-up using already available elements (nonlinear crystal, photodiode or spectrometer). In order to characterize the pulse entering the pulse shaper, the output of the nonlinear process is recorded for a sequence of different waveforms. Depending on the sequence of waveforms used, many different techniques can be implemented. Indeed, variants of both FROG [178–180] and SPIDER [160, 180, 181] have been implemented using this approach.

For instance FROG can be implemented by programming, using the shaper, a delayed replica sent to a nonlinear crystal ($\chi^{(2)}$). Recording the spectrum as a function of the delay gives an interferometric FROG (iFROG) trace. The classical FROG trace can be extracted by Fourier processing [178] (see figure 33(c)) or obtained directly using a calcite plate and type II crystal to avoid interferences [180]. Figure 33(a) taken from [178] shows the iFROG trace of a laser pulse passed through 5 cm of fused silica and acquired using a $4f$-line
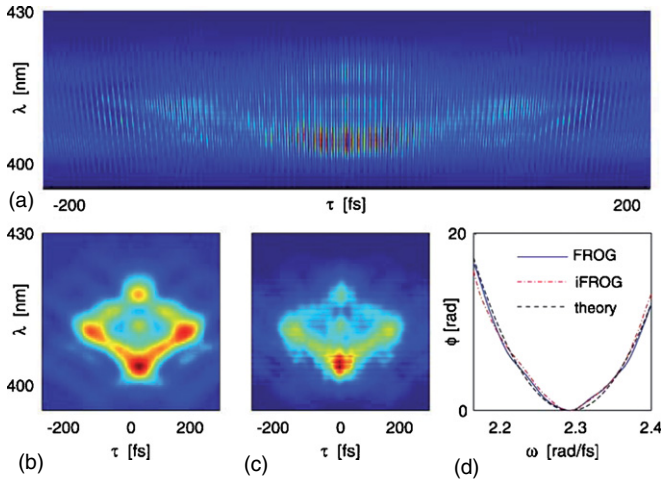
Figure 33. Taken from [178]. (a) iFROG measurements and (b) reference FROG. (c) FROG trace retrieved from (a). (d) Extracted phases from the FROG and iFROG traces of a laser pulse passed through 5 cm of fused silica.

shaper. The oscillations are typical of interferometric traces. A reference FROG trace has been measured in figure 33(b) for comparison whereas figure 33(c) is the FROG trace extracted from (a). Finally panel (d) shows the retrieved spectral phase for both iFROG and FROG techniques as well as theory.

What is more, using a pulse shaper opens the door to new possibilities that are not easily implemented using standard optics. This is the case of MIIPS (multiphoton intrapulse interference phase scan) [182–184] where the pulse shaper is used to add various known phase profiles to the test pulse. The output of the second-harmonic generation (SHG) is then spectrally resolved and recorded as a function of the added phase profiles.

It has been shown [184] that in the SHG spectra, a local maximum is observed when the total spectral phase is locally minimized. This occurs when its second derivative is equal to zero [184]:

$$\varphi_{\text{tot}}^{(2)}(\omega_m) = \varphi^{(2)}(\omega_m) + f^{(2)}(\omega_m) = 0 \qquad (55)$$

where $f(\omega)$ is the added phase function and ω_m is the frequency corresponding to the maximum of the SHG spectrum. As $f^{(2)}(\omega)$ is a known function one can determine $\varphi^{(2)}(\omega_m)$. By varying the applied function $f(\omega)$, one can retrieve $\varphi^{(2)}(\omega)$ across the whole spectrum and then reconstruct $\varphi(\omega)$ modulo a linear term. Figure 34 illustrates this principle using sets of quadratic phases as functions $f(\omega)$.

The solid line in panel (a) represents the unknown $\varphi^{(2)}(\omega)$ which is mapped using an horizontal grid of function $f^{(2)}$ corresponding here to different amount of linear chirp. The intersections of the solid line with the horizontal lines fulfil equation (55). In (b) the SHG spectrum is recorded and plotted as a function of ω for each function $f(\omega)$: each maximum corresponds to an intersection in (a) where the unknown phase is properly compensated for and thus measured. Plotting SHG intensity as a function of both chirp and frequency directly reveals the unknown phase $\varphi^{(2)}$ as shown in (c). Finally the number of functions $f(\omega)$ generable by a pulse shaper is vast
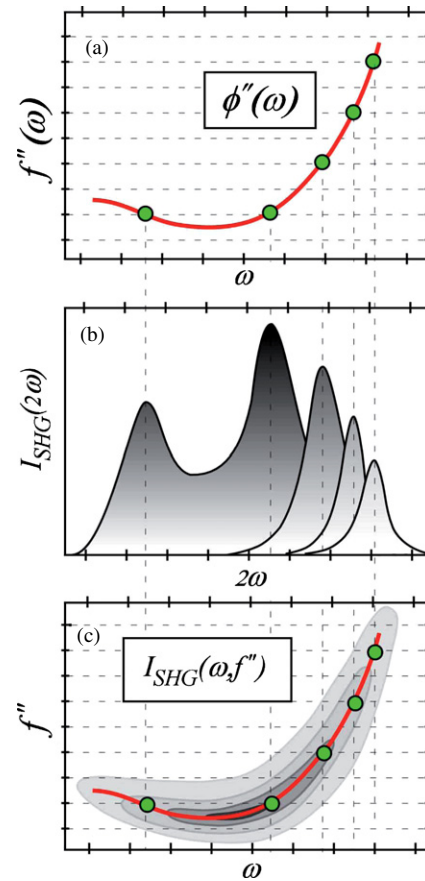

Figure 34. Taken from [185]. Principle of the MIIPS method. (a) The unknown $\phi''(\omega)$ function is probed using a set of reference linear chirps represented by the horizontal grid. (b) The maximum SHG intensity for every frequency indicates that the corresponding reference chirp value compensates the unknown function at the position of the maximum. (c) A two-dimensional contour plot mapping the intensity of the SHG as a function of chirp and frequency directly reveals the unknown $\phi''(\omega)$.

and leaves the choice for appropriate set of functions, like sinusoidal phases [182].

One major advantage of all the shaper-assisted characterization techniques is that the same set-up can be used to achieve several quasi-independent measurements of the same pulse, by simply changing the sequence of the waveforms used in order to implement different characterization techniques [178–180]. This constitutes a unique advantage of shaper-assisted characterization techniques over traditional ones where each technique relies on a dedicated experimental set-up.

One last advantage is that the resulting set-up is simple and straightforward as most of the complexity as been shifted to the pulse shaper and its programmed waveform. In particular, such a set-up does not involve any beam splitting or recombining and can thus be easily aligned and is compatible with *in situ* measurements.

Shaper-assisted characterization techniques are thus particularly interesting whenever a pulse shaper is available. Indeed, any pulse shaper may suffice (indeed, both AOPDF and $4f$ pulse shapers have been successfully used) and the

J. Phys. B: At. Mol. Opt. Phys. **43** (2010) 103001

PhD Tutorial

overhead for turning it into a versatile characterization set-up is close to zero. However, theses techniques should be used wisely. Indeed, most of the implementations require a perfectly calibrated pulse shaper, used within its range of validity. Moreover various measurements made with the same pulse shaper are not truly independent and cannot fully replace an independent cross-check.

6. General conclusion

In this tutorial, we have tried to give an overview of some of the most widespread techniques in ultrashort pulse shaping and characterization. This tutorial is by no means a complete review of but an introduction to two fast evolving fields of research. For any technique presented here, interested readers can find more details and in-depth discussion in the references provided. As a general conclusion, we would like to give one last piece of advice for both shaping and characterization. In both cases, it is crucial to keep in mind the range of validity, or the range of usage, out of which the result is not well determined. This piece of advice sounds elementary, but as shapers and characterization techniques tend to grow more complex and more subtle, it is not always straightforward to fully apprehend their limits. This is particularly true for shaper-assisted characterization techniques as one should stay within both the range of validity of the technique implemented and within the range of abilities of the shaper used.

Acknowledgments

References

To help tutorial readers prioritize the material they should become familiar with, the references have been rated * (additional material); ** (important literature); *** (essential reading); or not rated. These ratings should, under no circustances, be mistaken for quality ratings.

[1] DeMaria A J, Ferrar C M and Danielson G E Jr 1966 Mode locking of a Nd^{3+}-doped glass laser *Appl. Phys. Lett.* **8** 22–4
[2] Goswami D 2003 Optical pulse shaping approaches to coherent control. *Phys. Rep.* **374** 385
[3] Ohmori K 2009 Wave-packet and coherent control dynamics *Annu. Rev. Phys. Chem.* **60** 487–511
[4] Dantus M and Lozovoy V V 2004 Experimental coherent laser control of physicochemical processes *Chem. Rev.* **104** 1813–59
[5] Shim S-H and Zanni M T 2009 How to turn your pump-probe instrument into a multidimensional spectrometer: 2D IR and VIS spectroscopies via pulse shaping *Phys. Chem. Chem. Phys.* **11** 748–61

[6] Silberberg Y 2009 Quantum coherent control for nonlinear spectroscopy and microscopy *Annu. Rev. Phys. Chem.* **60** 277–92
[7] Efimov A, Moores M D, Mei B, Krause J L, Siders C W and Reitze D H 2000 Minimization of dispersion in an ultrafast chirped pulse amplifier using adaptive learning *Appl. Phys.* B **70** S133
[8] Weber S, Chatel B and Girard B 2008 Factoring numbers with interfering random waves *EuroPhys. Lett.* **83** 34008
[9] Bigourd D, Chatel B, Girard B and Schleich W P 2008 Factorization of numbers with the temporal Talbot effect: optical implementation by a sequence of shaped ultrashort pulses *Phys. Rev. Lett.* **100** 030202
[10] Sardesai H P, Chang C C and Weiner A M 1998 A femtosecond code division multiple-access communication system test bed *J. Lightwave Technol.* **16** 1953
[11] ***Weiner A M 2000 Femtosecond pulse shaping using spatial light modulators *Rev. Sci. Instrum.* **71** 1929–60
[12] ***Trebino R, DeLong K W, Fittinghoff D N, Sweetser J N, Krumbügel M A and Richman B A 1997 Measuring ultrashort laser pulses in the time-frequency domain using frequency-resolved optical gating *Rev. Sci. Instrum.* **68** 3277–95
[13] ***Walmsley I A and Dorrer C 2009 Characterization of ultrashort electromagnetic pulses *Adv. Opt. Photon.* **1** 308–437
[14] **Diels J C and Rudolph W 2006 *Ultrashort Laser Pulse Phenomena* 2nd edn
[15] **Wollenhaupt M, Assion A and Baumert T 2007 *Springer Handbook of Lasers and Optics* (Berlin: Springer) chapter 12, pp 937–83
[16] Hannaford P 2005 *Femtosecond Laser Spectroscopy*
[17] Krausz F and Ivanov M 2009 Attosecond physics *Rev. Mod. Phys.* **81** 163
[18] Chatel B, Degert J, Stock S and Girard B 2003 Competition between sequential and direct paths in a two-photon transition *Phys. Rev.* A **68** 041402
[19] Broers B, van Linden van den Heuvell H B and Noordam L D 1992 Efficient population transfer in a three-level ladder system by frequency-swept ultrashort laser pulses *Phys. Rev. Lett.* **69** 2062
[20] Broers B, Christian J F, Hoogenaard J H, van der Zande W J, van Linden van den Heuvell H B and Noordam L D 1993 Time-resolved dynamics of electronic wave packets above the classical field-ionisation threshold *Phys. Rev. Lett.* **71** 344
[21] Ventalon C, Fraser J M, Vos M H, Alexandrou A, Martin J-L and Joffre M 2004 Coherent vibrational climbing in carboxyhemoglobin *Proc. Natl Acad. Sci.* **101** 13216
[22] Chatel B, Degert J and Girard B 2004 Role of quadratic and cubic spectral phases in ladder climbing with ultrashort pulses *Phys. Rev.* A **70** 053414
[23] Cohen L 1989 Time-frequency distributions—a review *Proc. IEEE* **77** 941
[24] Paye J 1992 The chronocyclic representation of ultrashort light pulses *IEEE J. Quantum Electron.* **28** 2262–73
[25] ***Trebino R 2000 *Frequency-Resolved Optical Gating: The Measurement of Ultrashort Laser Pulses* (Dordrecht: Kluwer)
[26] Judson R S and Rabitz H 1992 Teaching lasers to control molecules *Phys. Rev. Lett.* **68** 1500–3
[27] Florean A C, Cardoza D, White J L, Lanyi J K, Sension R J and Bucksbaum P H 2009 Control of retinal isomerization in bacteriorhodopsin in the high-intensity regime *Proc. Natl Acad. Sci.* **106** 10896–900
[28] Savolainen J, Fanciulli R, Dijkhuizen N, Moore A L, Hauer J, Buckup T, Motzkus M and Herek J L 2008 Controlling the efficiency of an artificial light-harvesting complex *Proc. Natl Acad. Sci.* **105** 7641–6

[29] Brixner T, Damrauer N H, Niklaus P and Gerber G 2001 Photoselective adaptive femtosecond quantum control in the liquid phase *Nature* **414** 57–60

[30] Levis R J, Menkir G M and Rabitz H 2001 Selective bond dissociation and rearrangement with optimally tailored, strong-field laser pulses *Science* **292** 709–13

[31] Winterfeldt C, Spielmann C and Gerber G 2008 Colloquium: optimal control of high-harmonic generation *Rev. Mod. Phys.* **80** 117

[32] Cruz J M D, Pastirk I, Comstock M, Lozovoy V V and Dantus M 2004 Use of coherent control methods through scattering biological tissue to achieve functional imaging *Proc. Natl Acad. Sci.* **101** 16996–7001

[33] Assion A, Baumert T, Bergt M, Brixner T, Kiefer B, Seyfried V, Strehle M and Gerber G 1998 Control of chemical reactions by feedback-optimized phase-shaped femtosecond laser pulses *Science* **282** 919

[34] Nuernberger P, Vogt G, Brixner T and Gerber G 2007 Femtosecond quantum control of molecular dynamics in the condensed phase *Phys. Chem. Chem. Phys.* **9** 2470–97

[35] Monmayrant A, Chatel B and Girard B 2006 Atomic spirograph: measurement of the excited state wave function using coherent transients *Phys. Rev. Lett.* **96** 103002

[36] Degert J, Wohlleben W, Chatel B, Motzkus M and Girard B 2002 Realization of a time-domain Fresnel lens with coherent control *Phys. Rev. Lett.* **89** 203003

[37] Dudovich N, Dayan B, Faeder S M Gallagher and Silberberg Y 2001 Transform-limited pulses are not optimal for resonant multiphoton transitions *Phys. Rev. Lett.* **86** 47

[38] Dudovich N, Oron D and Silberberg Y 2002 Coherent transient enhancement of optically induced resonant transitions *Phys. Rev. Lett.* **88** 123004

[39] Amitay Z, Gandman A, Chuntonov L and Rybak L 2008 Multichannel selective femtosecond coherent control based on symmetry properties *Phys. Rev. Lett.* **100** 193002

[40] Pe'er A, Dayan B, Friesem A A and Silberberg Y 2005 Temporal shaping of entangled photons *Phys. Rev. Lett.* **94** 073601–4

[41] Walowicz K A, Pastirk I, Lozovoy V V and Dantus M 2002 Multiphoton intrapulse interference: I. Control of multiphoton processes in condensed phases *J. Phys. Chem. A* **106** 9369

[42] Martchenko T, Siedschlag C, Zamith S, Muller H G and Vrakking M J J 2005 Optimal control of femtosecond laser-cluster interactions *Phys. Rev. A* **72** 053202

[43] Bartelt A F, Feurer T and Woste L 2005 Understanding optimal control results by reducing the complexity *Chem. Phys.* **318** 207–16

[44] Dudovich N, Polack T, Pe'er A and Silberberg Y 2005 Simple route to strong-field coherent control *Phys. Rev. Lett.* **94** 083002

[45] Clow S D, Trallero-Herrero C, Bergeman T and Weinacht T 2008 Strong field multiphoton inversion of a three-level system using shaped ultrafast laser pulses *Phys. Rev. Lett.* **100** 233603

[46] Laarmann T, Shchatsinin I, Singh P, Zhavoronkov N, Gerhards M, Schulz C P and Hertel I V 2007 Coherent control of bond breaking in amino acid complexes with tailored femtosecond pulses *J. Chem. Phys.* **127** 201101

[47] de Nalda R, Horn C, Wollenhaupt M, Krug M, Banares L and Baumert T 2007 Pulse shaping control of alignment dynamics in n-2 *J. Raman Spectrosc.* **38** 543–50

[48] Ohmori K, Sato Y, Nikitin E E and Rice S A 2003 High-precision molecular wave-packet interferometry with HgAr dimers *Phys. Rev. Lett.* **91** 243003

[49] ***Walmsley I, Waxer L and Dorrer C 2001 The role of dispersion in ultrafast optics *Rev. Sci. Instrum.* **72** 1–29

[50] Treacy E B 1969 Optical pulse compression with diffraction gratings *IEEE J. Quantum Electron.* **5** 454–8

[51] Martinez O E 1987 3000 times grating compressor with positive group velocity dispersion: application to fiber compensation in 1.3–1.6 μm region *IEEE J. Quantum Electron.* **23** 59–64

[52] Szipocs R and Kohazi-Kis A 1997 Theory and design of chirped dielectric laser mirrors *Appl. Phys. B: Lasers Opt.* **65** 115

[53] **Steinmeyer G 2003 A review of ultrafast optics and optoelectronics *J. Opt. A: Pure Appl. Optics* **5** R1

[54] Froehly C, Colombeau B and Vampouille M 1983 Shaping and analysis of picosecond light pulses *Prog. opt.* **20** 65–153

[55] Weiner A M, Heritage J P and Kirschner E M 1988 High-resolution femtosecond pulse shaping *J. Opt. Soc. Am.* **5** 1563–72

[56] *Brixner T and Gerber G 2001 Femtosecond polarization pulse shaping *Opt. Lett.* **26** 557–9

[57] Feurer T, Vaughan J C, Koehl R M and Nelson K A 2002 Multidimensional control of femtosecond pulses by use of a programmable liquid-crystal matrix *Opt. Lett.* **27** 652–4

[58] **Danailov M B and Christov I P 1989 Time-space shaping of light pulses by fourier optical processing *J. Mod. Opt.* **36** 725–31

[59] Boyko O, Valentin C, Rey G, Antonucci L, Balcou Ph and Coudreau S 2005 Temporal superresolution of ultrashort laser pulses *Opt. Express* **13** 8222–30

[60] *Monmayrant A and Chatel B 2004 A new phase and amplitude high resolution pulse shaper *Rev. Sci. Instrum.* **75** 2668–71

[61] *Shim S H, Strasfeld D B, Fulmer E C and Zanni M T 2006 Femtosecond pulse shaping directly in the mid IR using acousto-optic modulation *Opt. Lett.* **31** 838

[62] Tanabe T, Tanabe H, Teramura Y and Kannari F 2002 Spatiotemporal measurements based on spatial spectral interferometry for ultrashort optical pulses shaped by a fourier pulse shaper *J. Opt. Soc. Am. B* **19** 2795–802

[63] **Wefers M M and Nelson K A 1995 Analysis of programmable ultrashort waveform generation using liquid-crystal spatial light-modulators *J. Opt. Soc. Am.* **12** 1343–62

[64] **Dorrer C and Salin F 1998 Phase amplitude coupling in spectral phase modulation *IEEE J. Select. Top. Quantum Electron.* **4** 342

[65] **Sussman B J, Lausten R and Stolow A 2008 Focusing of light following a 4-f pulse shaper: considerations for quantum control *Phys. Rev. A* **77** 043416

[66] Frei F, Galler A and Feurer T 2009 Space-time coupling in femtosecond pulse shaping and its effects on coherent control *J Chem. Phys.* **130** 034302

[67] Dudovich N, Oron D and Silberberg Y 2004 Quantum control of the angular momentum distribution in multiphoton absorption processes *Phys. Rev. Lett.* **92** 103003

[68] Efimov A, Schaffer C and Reitze D H 1995 Programmable shaping of ultrabroad-bandwidth pulses from a Ti:sapphire laser *J. Opt. Soc. Am.* **12** 1968–80

[69] Zeidler D, Hornung T, Proch D and Motzkus M 2000 Adaptive compression of tunable pulses from a non-collinear-type OPA to below 16 fs by feedback-controlled pulse shaping *Appl. Phys.* B **70** S125

[70] Wang H, Zheng Z, Leaird D E, Weiner A M, Dorschner T A, Fijol J J, Friedman L J, Nguyen H Q and Palmaccio L A 2001 20-fs pulse shaping with a 512-element phase-only liquid crystal modulator *IEEE J. Sel. Top. Quantum Electron.* **7** 718–27

[71] Yelin D, Meshulach D and Silberberg Y 1997 Adaptive femtosecond pulse compression *Opt. Lett.* **22** 1793–5

[72] Sofikitis D, Weber S, Fioretti A, Horchani R, Allegrini M, Chatel B, Comparat D and Pillet P 2009 Molecular

vibrational cooling by optical pumping with shaped femtosecond pulses *J. Phys.* **11** 055037

[73] Mermillod-Blondin A, Mauclair C, Rosenfeld A, Bonse J, Hertel I V, Audouard E and Stoian R 2008 Size correction in ultrafast laser processing of fused silica by temporal pulse shaping *Appl. Phys. Lett.* **93** 021921

[74] Vaughan J, Feurer T, Stone Katherine and Nelson K 2006 Analysis of replica pulses in femtosecond pulse shaping with pixelated devices *Opt. Express* **14** 1314

[75] Hillegas C W, Tull J X, Goswami D, Strickland D and Warren W S 1994 Femtosecond laser pulse shaping by use of microsecond radio-frequency pulses *Opt. Lett.* **19** 737

[76] **Dugan M A, Tull J X and Warren W S 1997 High-resolution acousto-optic shaping of unamplified and amplified femtosecond laser pulses *J. Opt. Soc. Am.* **14** 2348–58

[77] Chang I C 1976 I. Acoustooptic devices and applications *IEEE Trans. Sonics Ultrason.* **23** 2–21

[78] Roth M, Mehendale M, Bartelt A and Rabitz H 2005 Acousto-optical shaping of ultraviolet femtosecond pulses *Appl. Phys.* B **80** 441

[79] Fetterman M, Goswami D, Keusters D, Yang W, Rhee J-K and Warren W 1998 Ultrafast pulse shaping: amplification and characterization *Opt. Express* **3** 366–75

[80] Huang Yu and Dogariu A 2006 Application of adaptive feedback loop for ultra-violet femtosecond pulse shaper control *Opt. Express* **14** 10089–94

[81] Trallero-Herrero C, Cohen J L and Weinacht T C 2006 Strong field atomic phase matching *Phys. Rev. Lett.* **96** 063603

[82] Roth M, Guyon L, Roslund J, Boutou V, Courvoisier F, Wolf J-P and Rabitz H 2009 Quantum control of tightly competitive product channels *Phys. Rev. Lett.* **102** 253001–4

[83] Greenfield M, McGrane S D and Moore D S 2009 Control of cis-stilbene photochemistry using shaped ultraviolet pulses *J. Phys. Chem.* A **113** 2333–9

[84] Kotur M, Weinacht T, Pearson B J and Matsika S 2009 Closed-loop learning control of isomerization using shaped ultrafast laser pulses in the deep ultraviolet *J. Chem. Phys.* **130** 134311

[85] Shim S-H, Strasfeld D B and Zanni M T 2006 Generation and characterization of phase and amplitude shaped femtosecond mid IR pulses *Opt. Express* **14** 13120–30

[86] Weinacht T C, Ahn J and Bucksbaum P H 1998 Measurement of the amplitude and phase of a sculpted Rydberg wave packet *Phys. Rev. Lett.* **80** 5508

[87] Weinacht T C, Ahn J and Bucksbaum P H 1999 Controlling the shape of a quantum wavefunction *Nature* **397** 233

[88] Tian P, Keusters D, Suzaki Y and Warren W S 2003 Femtosecond phase-coherent two-dimensional spectroscopy *Science* **300** 1553–5

[89] Pearson B and Weinacht T C 2007 Shaped ultrafast laser pulses in the deep ultraviolet *Opt. Express* **17** 4385

[90] Zeek E, Maginnis K, Backus S, Russek U, Murnane M, Mourou G, Kapteyn H and Vdovin G 1999 Pulse compression by use of deformable mirrors *Opt. Lett.* **24** 493–5

[91] no Mejía J G, Greenaway A H and Reid D T 2004 Programmable spectral phase control of femtosecond pulses by use of adaptive optics and real-time pulse measurement *J. Opt. Soc. Am.* B **21** 833–43

[92] Hacker M, Stobrawa G, Sauerbrey R, Buckup T, Motzkus M, Wildenhain M and Gehner A 2003 Micromirror SLM for femtosecond pulse shaping in the ultraviolet *Appl. Phys.* B **76** 711–4

[93] Rondi A, Extermann J, Bonacina L, Weber S and Wolf J-P 2009 Characterization of a MEMS-based pulse-shaping device in the deep ultraviolet *Appl. Phys.* B **96** 757–61

[94] Möhring J, Buckup T, Lehmann C S and Motzkus M 2009 Generation of phase-controlled ultraviolet pulses and characterization by a simple autocorrelator setup *J. Opt. Soc. Am.* B **26** 1538–44

[95] Vaughan J C, Hornung T, Feurer T and Nelson K A 2005 Diffraction-based femtosecond pulse shaping with a two-dimensional spatial light modulator *Opt. Lett.* **30** 323–5

[96] *Frumker E and Silberberg Y 2007 Phase and amplitude pulse shaping with two-dimensional phase-only spatial light modulators *J. Opt. Soc. Am.* B **24** 2940

[97] Tanigawa T, Sakakibara Yu, Fang S, Sekikawa T and Yamashita M 2009 Spatial light modulator of 648 pixels with liquid crystal transparent from ultraviolet to near-infrared and its chirp compensation application *Opt. Lett.* **34** 1696–8

[98] Tan H S, Warren W S and Schreiber E 2001 Generation and amplification of ultrashort shaped pulses in the visible by a two-stage noncollinear optical parametric process *Opt. Lett.* **26** 1812

[99] Fermann M E, da Silva V, Smith D A, Silberberg Y and Weiner A M 1993 Shaping of ultrashort optical pulses by using an integrated acousto-optic tunable filter *Opt. Lett.* **18** 1505–7

[100] **Verluise F, Laude V, Cheng Z, Spielmann C and Tournois P 2000 Amplitude and phase control of ultrashort pulses by use of an acousto-optic programmable dispersive filter: pulse compression and shaping *Opt. Lett.* **25** 575

[101] *Coudreau S, Kaplan D and Tournois P 2006 Ultraviolet acousto-optic programmable dispersive filter laser pulse shaping in KDP *Opt. Lett.* **31** 1899

[102] **Kaplan D and Tournois P 2002 Theory and performance of the acousto optic programmable dispersive filter used for femtosecond laser pulse shaping *J. Phys. IV* **12** Pr5–69

[103] Seres J, Müller A, Seres E, O'Keeffe K, Lenner M, Herzog R F, Kaplan D, Spielmann C and Krausz F 2003 Sub-10-fs, terawatt-scale Ti:sapphire laser system *Opt. Lett.* **28** 1832–4

[104] Monmayrant A, Arbouet A, Girard B, Chatel B, Whitaker B J, Barman A and Kaplan D 2005 Optimisation of NOPA output pulse shaping using an AOPDF with dispersion self-correction *Appl. Phys.* B **81** 177

[105] Reitze D H *et al* 2004 Enhancement of high-order harmonic generation at tuned wavelengths through adaptive control *Opt. Lett.* **29** 86–8

[106] Papadopoulos D N, Hanna M, Druon F and Georges P 2008 Active spectral phase control by use of an acousto-optic programmable filter in high-repetition rate sub-80 fs nonlinear fiber amplifiers *Opt. lett.* **33** 1431

[107] Form N T, Whitaker J B C and Meier C 2008 Enhancing the probability of three-photon absorption in iodine through pulse shaping *J. Phys. B: At. Mol. Opt. Phys.* **41** 074011

[108] Weber S, Barthelemy M and Chatel B 2009 Direct shaping of tunable UV ultrashort pulses *Appl. Phys.* B **98** 323–6

[109] Tournois P 2008 Design of acousto-optic programmable filters in mercury halides for mid-infrared laser pulse shaping *Opt. Commun.* **281** 4054

[110] Form N T, Burbidge R, Ramon J and Whitaker B J Parameterization of an acousto-optic programmable dispersive filter for closed-loop learning experiments *J. Mod. Opt.* **55** 197–209

[111] Belabas N, Likforman J P, Canioni L, Bousquet B and Joffre M 2001 Coherent broadband pulse shaping in the mid infrared *Opt. Lett.* **26** 743–5

[112] Kaindl R A, Wurm M, Reimann K, Hamm P, Weiner A M and Woerner M 2000 Generation, shaping, and characterization of intense femtosecond pulses tunable from 3 to 20 μm *J. Opt. Soc. Am.* B **17** 2086–94

J. Phys. B: At. Mol. Opt. Phys. **43** (2010) 103001

PhD Tutorial

[113] Hacker M, Feurer T, Sauerbrey R, Lucza T and Szabo G
2001 Programmable femtosecond laser pulses in the
ultraviolet *J. Opt. Soc. Am.* **18** 866–71

[114] **Schriever C, Lochbrunner S, Optiz M and Riedle E 2006
19 fs shaped ultraviolet pulses *Opt. Lett.* **31** 543

[115] Broers B, Vandenheuvell H B V and Noordam L D 1992
Large interference effects of small chirp observed in
2-photon absorption *Opt. Commun.* **91** 57

[116] Koller F O, Haiser K, Huber M, Schrader T E, Regner N,
Schreier W J and Zinth W 2007 Generation of narrowband
subpicosecond midinfrared pulses via difference frequency
mixing of chirped near-infrared pulses *Opt. Lett.*
32 3339

[117] Raoult F, Boscheron A C L, Husson D, Sauteret C,
Modena A, Malka V, Dorchies F and Migus A 1998
Efficient generation of narrow-bandwidth picosecond
pulses by frequency doubling of femtosecond chirped
pulses *Opt. Lett.* **23** 1117

[118] Zeidler D, Witte T, Proch D and Motzkus M 2001 Optical
parametric amplification of a shaped white-light
continuum *Opt. Lett.* **26** 1921–3

[119] Wefers M M and Nelson K A 1993 Programmable phase and
amplitude femtosecond pulse shaping *Opt. Lett.* **18** 2032

[120] Präkelt A, Wollenhaupt M, Assion A, Horn C,
Sarpe-Tudoran C, Winter M and Baumert T 2003
Compact, robust and flexible setup for femtosecond pulse
shaping *Rev. Sci. Instrum.* **74** 4950

[121] Stobrawa G, Hacker M, Feurer T, Zeidler D, Motzkus M
and Reichel F 2001 A new high-resolution femtosecond
pulse shaper *Appl. Phys.* B **72** 627–30

[122] Binhammer T, Rittweger E, Ell R, Kartner F X and
Morgner U 2005 Prism-based pulse shaper for octave
spanning spectra *IEEE J. Quantum Electron.* **41** 1552–7

[123] Xu L, Nakagawa N, Morita R, Shigekawa H and
Yamashita M 2000 Programmable chirp compensation for
6-fs pulse generation with a prism-pair-formed pulse
shaper *IEEE J. Quantum Electron.* **36** 893–9

[124] Selle R, Nuernberger P, Langhojer F, Dimler F, Fechner S,
Gerber G and Brixner T 2008 Generation of polarization-
shaped ultraviolet femtosecond pulses *Opt. Lett.*
33 803–5

[125] Witte T, Zeidler D, Proch D, Kompa K L and Motzkus M
2002 Programmable amplitude and phase-modulated
femtosecond laser pulses in the mid-infrared *Opt. Lett.*
27 131–3

[126] Tan H-S and Warren W 2003 Mid infrared pulse shaping by
optical parametric amplification and its application to
optical free induction decay measurement *Opt. Express*
11 1021–8

[127] **Dudley J M, Walmsley I A and Trebino R 2008
Measurement of ultrashort electromagnetic pulses *J. Opt.
Soc. Am.* B **25** MU1–2

[128] Sala K, Kenney-Wallace G and Hall G 1980 Cw
autocorrelation measurements of picosecond laser pulses
IEEE J. Quantum Electron. **16** 990–6

[129] Diels J-C M, Fontaine J J, McMichael Ian C and Simoni F
1985 Control and measurement of ultrashort pulse shapes
(in amplitude and phase) with femtosecond accuracy *Appl.
Opt.* **24** 1270–82

[130] Monmayrant A, Chatel B and Girard B 2006 Real time
quantum state holography using coherent transients *Opt.
Commun.* **264** 256

[131] Goulielmakis E *et al* 2004 Direct measurement of light waves
Science **305** 1267–9

[132] Froehly C, Lacourt A and Vienot J C 1973 Notions de
réponse impulsionnelle et de fonction de transfert
temporelles des pupilles optiques *J. d'optique* **4** 183

[133] Takeda M, Ina H and Kobayashi S 1982 Fourier-transform
method of fringe-pattern analysis for computer-based
topography and interferometry *J. Opt. Soc. Am.* **72** 156–60

[134] **Lepetit L, Cheriaux G and Joffre M 1995 Linear
techniques of phase measurement by femtosecond spectral
interferometry for applications in spectroscopy *J. Opt.
Soc. Am* B **12** 2467

[135] Dorrer C and Joffre M 2001 Characterization of the spectral
phase of ultrashort light pulses *Académie des Sciences*
2 1415

[136] ***Kane D J and Trebino R 1993 Characterization of
arbitrary femtosecond pulses using frequency-resolved
optical gating *IEEE J. Quantum Electron.*
29 571–9

[137] Kane D J and Trebino R 1993 Single-shot measurement of
the intensity and phase of an arbitrary ultrashort pulse by
using frequency-resolved optical gating *Opt. Lett.*
18 823–5

[138] *Kane D J 1999 Recent progress toward real-time
measurement of ultrashort laser pulses *IEEE J. Quantum
Electron.* **35** 421

[139] Paye J, Ramaswamy M, Fujimoto J G and Ippen E P 1993
Measurement of the amplitude and phase of ultrashort
light pulses from spectrally resolved autocorrelation *Opt.
Lett.* **18** 1946

[140] O'Shea P, Kimmel M, Gu X and Trebino R 2001 Highly
simplified device for ultrashort-pulse measurement *Opt.
Lett.* **26** 932–4

[141] Reid D T, Loza-Alvarez P, Brown C T A, Beddard T
and Sibbett W 2000 Amplitude and phase measurement of
mid-infrared femtosecond pulses by using
cross-correlation frequency-resolved optical gating *Opt.
Lett.* **25** 1478–80

[142] Linden S, Kuhl J and Giessen H 1999 Amplitude and phase
characterization of weak blue ultrashort pulses by
downconversion *Opt. Lett.* **24** 569

[143] Tsubouchi M and Momose T 2009 Cross-correlation
frequency-resolved optical gating for mid-infrared
femtosecond laser pulses by an AgGaGeS$_4$ crystal *Opt.
Lett.* **34** 2447–9

[144] Dudley J, Xun Gu, Lin Xu, Kimmel M, Zeek E, O'Shea P,
Trebino R, Coen S and Windeler R 2002 Cross-correlation
frequency resolved optical gating analysis of broadband
continuum generation in photonic crystal fiber:
simulations and experiments *Opt. Express* **10** 1215–21

[145] Tsang T Y F, Krumbugel M A, DeLong K W,
Fittinghoff D N and Trebino R 1996 Frequency-
resolved optical-gating measurements of ultrashort pulses
using surface third-harmonic generation *Opt. Lett.*
21 1381–3

[146] Mairesse Y and Quere F 2005 Frequency-resolved optical
gating for complete reconstruction of attosecond bursts
Phys. Rev. A **71** 011401

[147] DeLong K W, Trebino R, Hunter J and White W E 1994
Frequency-resolved optical gating with the use of
second-harmonic generation *J. Opt. Soc. Am.* B
11 2206–15

[148] Akturk S, Kimmel M, Trebino R, Naumov S, Sorokin E
and Sorokina I 2003 Measuring several-cycle 1.5-m pulses
using frequency-resolved optical gating *Opt. Express*
11 3461–6

[149] Richman B A, Krumbügel M A and Trebino R 1997
Temporal characterization of mid IR free-electron-laser
pulses by frequency-resolved optical gating *Opt. Lett.*
22 721–3

[150] Stibenz G and Steinmeyer G 2005 Interferometric
frequency-resolved optical gating *Opt. Express*
13 2617–26

[151] Sweetser J N, Fittinghoff D N and Trebino R 1997
Transient-grating frequency-resolved optical gating *Opt.
Lett.* **22** 519–21

[152] Lee D, Akturk S, Gabolde P and Trebino R 2007
Experimentally simple, extremely broadband

J. Phys. B: At. Mol. Opt. Phys. **43** (2010) 103001

PhD Tutorial

transient-grating frequency-resolved-optical-gating arrangement *Opt. Express* **15** 760–6

[153] Iaconis C and Walmsley I A 1998 Spectral phase interferometry for direct electric-field reconstruction of ultrashort optical pulses *Opt. Lett.* **23** 792–4

[154] ***Anderson M E, Monmayrant A, Gorza S-P, Wasylczyk P and Walmsley I A 2008 Spider: a decade of measuring ultrashort pulses *Laser Phys. Lett.* **5** 259–66

[155] Hirasawa M, Nakagawa N, Yamamoto K, Morita R, Shigekawa H and Yamashita M 2002 Sensitivity improvement of spectral phase interferometry for direct electric-field reconstruction for the characterization of low-intensity femtosecond pulses *Appl. Phys.* B **74** s225

[156] Stibenz G and Steinmeyer G 2004 High dynamic range characterization of ultrabroadband white-light continuum pulses *Opt. Express* **12** 6319–25

[157] Dorrer C, Londero P and Walmsley I A 2001 Homodyne detection in spectral phase interferometry for direct electric field reconstruction *Opt. Lett.* **26** 1510

[158] Baum P, Lochbrunner S and Riedle E 2004 Zero-additional-phase spider: full characterization of visible and sub-20-fs ultraviolet pulses *Opt. Lett.* **29** 210–2

[159] **Baum P and Riedle E 2005 Design and calibration of zero-additional-phase spider *J. Opt. Soc. Am.* B **22** 1875–83

[160] Monmayrant A, Joffre M, Oksenhendler T, Herzog R, Kaplan D and Tournois P 2003 Time-domain interferometry for direct electric-field reconstruction by use of an acousto-optic programmable filter and a two-photon detector *Opt. Lett.* **28** 278

[161] Ventalon C, Fraser J M and Joffre M 2003 Time-domain interferometry for direct electric field reconstruction of mid-infrared femtosecond pulses *Opt. Lett.* **28** 1826–8

[162] Kosik E M, Radunsky A S, Walmsley I A and Dorrer C 2005 Interferometric technique for measuring broadband ultrashort pulses at the sampling limit *Opt. Lett.* **30** 326–8

[163] Gorza S P, Wasylczyk P and Walmsley I A 2007 Spectral shearing interferometry with spatially chirped replicas for measuring ultrashort pulses *Opt. Express* **15** 15168–74

[164] Bethge J, Grebing C and Steinmeyer G 2007 A fast gabor wavelet transform for high-precision phase retrieval in spectralinterferometry *Opt. Express* **15** 14313–21

[165] Bethge J and Steinmeyer G 2008 Numerical fringe pattern demodulation strategies in interferometry *Rev. Sci. Instrum.* **79** 073102

[166] Gallmann L, Sutter D H, Matuschek N, Steinmeyer G, Keller U, Iaconis C and Walmsley I A 1999 Characterization of sub-6-fs optical pulses with spectral phase interferometryfor direct electric-field reconstruction *Opt. Lett.* **24** 1314–6

[167] Dorrer C 1999 Implementation of spectral phase interferometry for direct electric-field reconstruction with a simultaneously recorded reference interferogram. *Opt. Lett.* **24** 1532–4

[168] Stibenz G and Steinmeyer G 2006 Optimizing spectral phase interferometry for direct electric-field reconstruction *Rev. Sci. Instrum.* **77** 073105

[169] Londero P, Anderson M E, Radzewicz C, Iaconis C and Walmsley I A 2003 Measuring ultrafast pulses in the near-ultraviolet using spectral phase interferometry for direct electric field reconstruction *J. Mod. Opt.* **50** 179–84

[170] Dorrer C and Kang I 2003 Highly sensitive direct characterization of femtosecond pulses by electro-optic spectral shearing interferometry *Opt. Lett.* **28** 477–9

[171] Kang I, Dorrer C and Quochi F 2003 Implementation of electro-optic spectral shearing interferometry for ultrashort pulse characterization *Opt. Lett.* **28** 2264–6

[172] Kubarych K J, Joffre M, Moore A, Belabas N and Jonas D M 2005 Mid-infrared electric field characterization using a visible charge-coupled-device-based spectrometer *Opt. Lett.* **30** 1228–30

[173] Mairesse Y, Gobert O, Breger P, Merdji H, Meynadier P, Monchicourt P, Perdrix M, Salieres P and Carre B 2005 High harmonic XUV spectral phase interferometry for direct electric-field reconstruction *Phys. Rev. Lett.* **94** 173903

[174] *Wyatt A S, Walmsley I A, Stibenz G and Steinmeyer G 2006 Sub-10 fs pulse characterization using spatially encoded arrangement for spectral phase interferometry for direct electric field reconstruction *Opt. Lett.* **31** 1914–6

[175] Radunsky A S, Walmsley I A, Gorza S P and Wasylczyk P 2007 Compact spectral shearing interferometer for ultrashort pulse characterization *Opt. Lett.* **32** 181–3

[176] Birge J R, Ell R and Kärtner F X 2006 Two-dimensional spectral shearing interferometry for few-cycle pulse characterization *Opt. Lett.* **31** 2063–5

[177] Foing J-P, Likforman J-P, Joffre M and Migus A 1992 Femtosecond pulse phase measurement by spectrally resolved up-conversion: application to continuum compression *IEEE J. Quantum Electron.* **28** 2285–90

[178] Galler A and Feurer T 2008 Pulse shaper assisted short laser pulse characterization *Appl. Phys.* B **90** 427–30

[179] Forget N, Coudreau S, Lepetit F, Albert O and Oksenhendler T 2007 Achromatic and single-beam pulse characterization technique for visible-UV pulses based on direct UV pulse shaping and cross-polarized wave generation. *CLEO/Europe and IQEC 2007 Conference Digest (Optical Society of America)* p CF4_5.

[180] Forget N, Joffre M, Coudreau S and Oksenhendler T 2007 Toward programmable ultrashort pulse characterization. *CLEO/Europe and IQEC 2007 Conference Digest (Optical Society of America)* p CF_16.

[181] von Vacano B, Buckup T and Motzkus M 2007 Shaper-assisted collinear spider: fast and simple broadband pulse compression in nonlinear microscopy *J. Opt. Soc. Am.* **24** 1091–100

[182] Coello Y, Lozovoy V V, Gunaratne T C, Bingwei Xu, Borukhovich I, Tseng C-H, Weinacht Thomas and Dantus M 2008 Interference without an interferometer: a different approach to measuring, compressing, and shaping ultrashort laser pulses *J. Opt. Soc. Am.* B **25** A140–50

[183] Bingwei Xu, Coello Y, Lozovoy V V, Harris D A and Dantus Marcos 2006 Pulse shaping of octave spanning femtosecond laser pulses *Opt. Express* **14** 10939–44

[184] Lozovoy V V, Pastirk I and Dantus M 2004 Multiphoton intrapulse interference: iv. Ultrashort laser pulse spectral phase characterization and compensation *Opt. Lett.* **29** 775

[185] Lozovoy V V, Bingwei Xu, Coello Y and Dantus M 2008 Direct measurement of spectral phase for ultrashort laser pulses *Opt. Express* **16** 592–7